A. Soltani, A. Deng, A. Taheri, M. Mirzababaei, H. Nikraz
Interfacial shear strength of rubber-reinforced clays: a dimensional analysis perspective
Geosynthetics International, 2019; 26(2):164-183

Version of record: http://dx.doi.org/10.1680/jgein.18.00045

Accepted manuscript doi:
10.1680/jgein.18.00045

Submitted: 29 January 2018

Published online in 'accepted manuscript' format: 16 November 2018

Manuscript title: Interfacial Shear Strength of Rubber–Reinforced Clays: A Dimensional Analysis Perspective

Authors: A. Soltani[1], A. Deng[1], A. Taheri[1], M. Mirzababaei[2] and H. Nikraz[3]

Affiliations: [1]School of Civil, Environmental and Mining Engineering, The University of Adelaide, Adelaide, SA 5005, Australia; [2]School of Engineering and Technology, Central Queensland University, Melbourne, VIC 3000, Australia and [3]School of Civil and Mechanical Engineering, Curtin University, Perth, WA 6102, Australia

Corresponding author: Amin Soltani, School of Civil, Environmental and Mining Engineering, The University of Adelaide, Adelaide, SA 5005, Australia. Tel.: +61498254050.

E-mail: Amin.Soltani@adelaide.edu.au

Accepted manuscript doi:
10.1680/jgein.18.00045

Abstract

The present study aims towards the development of practical dimensional models capable of simulating the interfacial shear strength of rubber–reinforced clays. Two types of recycled tire rubbers (of fine and coarse categories) were each incorporated into the soil at four different contents (by weight), and statically compacted at their respective Proctor optimum condition for direct shear testing. The rubber inclusions amended the soil through improvements achieved in two aspects: i) frictional resistance generated as a result of soil–rubber contact; and ii) mechanical interlocking of rubber particles and soil grains. In general, both amending mechanisms were in favor of a higher rubber content, and to a lesser degree a larger rubber size. The dimensional analysis concept was extended to the soil–rubber shear strength problem, thereby leading to the development of practical dimensional models capable of simulating the shear stress–horizontal displacement response as a function of the composite's basic index properties. The predictive capacity of the proposed models was examined and validated by statistical techniques. The proposed dimensional models contain a limited number of fitting parameters, which can be calibrated by minimal experimental effort and hence implemented for predictive purposes.

Keywords: Geosynthetics; Rubber–reinforced clay; Interfacial shear strength; Frictional resistance; Mechanical interlocking; Dimensional analysis

Accepted manuscript doi:
10.1680/jgein.18.00045

1. Introduction

Sustainability in civil engineering is sought as a strategic step towards improving the mechanical performance of construction materials while counteracting the adverse environmental impacts associated with human activities. Solid waste materials are bulky in nature, owing to their low weight–to–volume ratio, and thus consume valuable landfill space upon disposal. To minimize the need for landfilling, local communities and governmental agencies have been increasingly encouraged to recycle and hence reuse such materials as part of the infrastructure system. As of late, many developed and developing countries have initiated the transition towards 'sustainable infrastructure', a concept which encourages the replacement of conventional quarried materials with solid wastes and/or industrial by–products (e.g. waste textiles/fibers, demolition wastes, kiln dusts, silicate/calcium chloride geopolymers and sulfonated oils), thereby conserving natural resources as well as reducing the level of greenhouse gas emissions. In this context, a number of research works have suggested innovative and environmentally sound solutions targeting the application of such materials in various civil engineering projects such as pavement construction, soil stabilization, concrete manufacturing and thermal insulations (e.g. Kim et al. 2008; Yesilata et al. 2009; Puppala et al. 2011; Briga-Sá et al. 2013; Mirzababaei et al. 2013[a], 2013[b]; Parghi and Alam 2016; Arulrajah et al. 2017; Hoy et al. 2017; Kua et al. 2017; Mirzababaei et al. 2018[a]; Soltani et al. 2017[a], 2018[a]). Beneficial reuse of waste resources not only intends to enhance infrastructure performance, but also encourages recycling, mitigates the burden (or hazard) on the environment and assists waste management by preventing the accumulation of bulky waste materials which are normally stored or landfilled without proper utilization. As such, any attempt to assimilate waste resources as part of the infrastructure system is at the forefront of many researchers and governmental authorities.

Discarded tires are amongst the largest and most problematic sources of solid waste, owing to extensive production and their durability over time. Such materials, as an ever–producing consumable element of modern life, constitutes for a large volume of disposals throughout the world. In Australia, for instance, it has been estimated that 48 million waste tires (i.e. equivalent to approximately 381,000 tons) are generated per annum (Hannam 2014). A major challenge has therefore been the space required for storing and transporting such waste materials, and the resulting costs (Thomas et al. 2016; Yadav and Tiwari 2017[a]). Quite clearly, discarded tires are not desired at landfills, due to their low weight–to–volume ratio, durability and resilient behavior, which prevents them from being 'flat–packed'. Those characteristics which make waste tires such a problem while being landfilled, make them one of the most reusable waste materials for the construction of sustainable earth backfills, thereby serving a variety of infrastructure needs, e.g. embankments, retaining walls and bridge abutments (Tweedie et al. 1998; Shalaby and Khan 2002; Yoon et al. 2006; Tanchaisawat et al. 2010; Li et al. 2016). Similar to fiber–reinforced soils, the rubber assemblage randomly distributes in the soil regime, and due to its rough surface texture, elastic character and low water adsorption capacity, engenders a spatial three–dimensional reinforcement network in favor of weaving (or interlocking) the soil grains into a coherent matrix of induced strength, improved ductility and deduced heave/settlement, thereby enhancing the integrity and stability of the infrastructure (e.g. Edil and Bosscher 1994; Zornberg et al. 2004; Cetin et al. 2006; Özkul and Baykal 2007; Tsoi and Lee 2011; Trouzine et al. 2012; Kalkan 2013; Cabalar and Karabash 2015; Signes et al. 2016; Perez et al. 2017; Yadav and Tiwari 2017[b]; Soltani et al. 2018[b], 2018[c]).

Accepted manuscript doi:
10.1680/jgein.18.00045

The advantages of soil–rubber composites in engineering performance, which conventional soil backfills rarely exhibit, are favorably promoting the sustainability of infrastructure systems. With the soil–rubber composite gaining ground as a viable geomaterial in practice, the need for an efficient and simple tool to adequately predict its short–term performance under field conditions, mainly in terms of shear strength, arises as an inevitable necessity. Such a toolbox, if developed, would aid the geotechnical engineer to arrive at reliable soil–rubber design choices without the hurdles of conducting time–consuming experimental tests. In this context, a limited number of discrete element models have been proposed, which adequately simulate the interfacial shear strength of rubber–reinforced sands (e.g. Youwai and Bergado 2004; Valdes and Evans 2008; Huggins and Ravichandran 2011; Lee et al. 2014; Perez et al. 2016; Wang et al. 2018). These studies gained insight into the inter–particle interactions, and demonstrated the role of rubber particles in changing the material fabrics and the material stiffness. Moreover, the use of artificial intelligence, e.g. neural networks, fuzzy logic systems and combined neuro–fuzzy approaches, has also shown great promise in describing/simulating the sand–rubber interactions (e.g. Edinclilera et al. 2012, 2013). To the authors' knowledge, there have been no attempts to extend the current numerical or constitutive literature to the clay–rubber shear strength problem. Nonetheless, such models, even if developed for the clay–rubber interface, would most certainly suffer from long–lasting and sophisticated calibration procedures, thus leading to impractical frameworks which are not trivial to implement for practicing engineers.

The present study aims towards the development of simple and practical dimensional models, by means of the dimensional analysis concept (Buckingham 1914), capable of simulating the interfacial shear strength of rubber–reinforced clays. Undrained direct shear tests were carried out on various compacted clay–rubber composites (with different consistency limits and initial placement conditions) to generate a reliable database allowing for the validation of the proposed dimensional models. The novel dimensional analysis practiced in this study led to a practical shear strength predicting toolbox by incorporating the composite's basic index properties, thereby avoiding the hurdles of conducting time–consuming experimental tests.

2. Experimental Work

2.1. Materials

2.1.1. Clay Soil

A mixture of 85% kaolinite and 15% sodium–activated bentonite, hereafter simply referred to as soil, was used for the experimental program. Physical and mechanical properties of the soil, determined as per relevant ASTM and Australian (AS) standards, are summarized in Table 1. The conventional grain–size analysis, carried out in accordance with ASTM D422 (2007), indicated a clay fraction (< 2 μm) of 52.80%, along with 46.16% silt (2–75 μm) and 1.04% fine sand (0.075–0.425 mm) (see Figure 1). The liquid limit and plasticity index were, respectively, measured as w_L=59.60% and I_P=32.32%, from which the soil was characterized as *clay with high plasticity* (CH) in accordance with the Unified Soil Classification System (USCS). The free swell ratio was obtained as FSR=2.91, from which the soil was graded as *highly expansive* with respect to the classification criterion suggested by Prakash and Sridharan (2004).

Accepted manuscript doi:
10.1680/jgein.18.00045

2.1.2. Tire Rubbers

Two types of commercially available recycled tire rubbers (of fine and coarse categories), commonly traded as rubber crumbs (or ground rubber) and rubber buffings, were used as the reinforcements. Hereafter, these rubber types will be referred to as Rubbers C and B, respectively. The gradation curve for both rubber types was determined as per ASTM D422 (2007), and the results are shown in Figure 1. The particles of Rubber C were analogous in size to fine–medium sand (0.075–2 mm), whereas Rubber B was graded into the medium–coarse sand category (0.425–4.75 mm). The particle diameters corresponding to 10%, 30%, 50% and 60% finer (or passing) were measured as d_{10}=0.182 mm and 1.077 mm, d_{30}=0.334 mm and 1.370 mm, d_{50}=0.478 mm and 1.582 mm, and d_{60}=0.513 mm and 1.682 mm for Rubbers C and B, respectively (see Figure 1). In addition, the coefficients of uniformity (i.e. $C_u=d_{60}/d_{10}$) and curvature (i.e. $C_c=d_{30}^2/d_{10}d_{60}$) were measured as C_u=2.81 and C_c=1.20 for Rubber C, and C_u=1.56 and C_c=1.04 for Rubber B, from which both rubber types were characterized as *poorly–graded* in accordance with the USCS criterion. Figure 2 illustrates microscopic micrographs of the rubber particles at different magnification ratios. The rubber particles are non–spherical and irregular in shape (see Figures 2b and 2e at 50x magnification), with some cavities and micro–cracks propagated along the rubber's surface (see Figures 2c and 2f at 200x magnification), thus making for a rough surface texture. Such surface characteristics could potentially promote adhesion and/or induce frictional resistance between the rubber particles and the soil grains, thereby alter the soil fabric into a coherent matrix of induced strength and improved ductility (Yadav and Tiwari 2017[b]; Soltani et al. 2018[b], 2018[d]). Other physical properties, as provided by the manufacturer, included a specific gravity (at 20 ^{o}C) of 1.09 and a softening point of 170 ^{o}C for both rubber types.

2.2. Compaction Studies and Sample Preparation

Both rubber choices were incorporated into the soil at four different rubber–to–dry soil weight ratios (or rubber contents), i.e. R_c=5%, 10%, 20% and 30%. A series of standard Proctor compaction tests were carried out on the natural soil, i.e. R_c=0%, and various soil–rubber mixtures in accordance with ASTM D698 (2012), and the results are provided in Table 2. For a given rubber type, the higher the rubber content the lower the compaction characteristics, following a monotonic decreasing trend. For a given rubber content, however, the effect of rubber size was observed to be marginal. Such trends can be attributed to the lower specific gravity, specific surface area and water adsorption capacity of the rubber particles compared with the soil grains (Özkul and Baykal 2007; Signes et al. 2016; Yadav and Tiwari 2017[b]; Soltani et al. 2018[b], 2018[c]). Moreover, the elastic (or rebound) response of rubber particles to dynamic energy during compaction may potentially reduce the compaction efficiency, and thus contribute to a lower maximum dry unit weight (Yadav and Tiwari 2017[b]; Soltani et al. 2018[d]). It should be noted that rubber–clustering effects were vigorously evident at rubber contents greater than 30%, which led to compactability issues as well as difficulties in achieving homogeneous soil–rubber mixtures. As such, rubber contents greater than 30% were not considered in the present study. Samples for the direct shear tests (see Section 2.3) were prepared by the static compaction technique, as described in Soltani et al. (2017[b]) and Estabragh et al. (2018), at the respective optimum water content and maximum dry unit weight of each mixture (i.e. w_{opt} and γ_{dmax} in Table 2). The required amount of water corresponding to the desired optimum water content was added to each mixture, and thoroughly mixed by hand. The mixtures were then enclosed in plastic bags and stored under

Accepted manuscript doi:
10.1680/jgein.18.00045

room temperature conditions for 24 hours, thus ensuring an even distribution of moisture throughout the composite mass. The moist mixtures were statically compressed in the shear box (measuring 60 mm×60 mm in plane and 20 mm in height) at three layers, each layer having attained the desired maximum dry unit weight.

Basic index properties of the prepared samples, including the consistency limits and the compaction characteristics, are summarized in Table 2. The natural soil and various soil–rubber mixtures were tested for consistency limits following the Australian code of practice (see relevant standard designations in Table 1). The liquid limit was obtained by means of the cone penetration method, while the conventional rolling thread technique was adopted for plastic limit measurements. The water content at which a mass of soil (or material) begins to crumble when manually rolled into a thread of approximately 3.2 mm (in diameter) is conventionally taken as the plastic limit. However, it is well accepted that the effect of thread diameter over a range of 2–6 mm is negligible (Prakash et al. 2009). Therefore, to accommodate the inclusion of rubber particles, which for some particles of Rubber B could measure as high as 3.2 mm in size, the rolling thread technique was implemented to threads of approximately 5 mm (in diameter). The higher the rubber content the lower the consistency limits, following a monotonic decreasing trend. The effect of rubber size, however, was found to be marginal. Similar to the optimum water content, reduction in the consistency limits can be attributed to the lower specific surface area and water adsorption capacity of the rubber particles compared with the soil grains (Cetin et al. 2006; Trouzine et al. 2012; Soltani et al. 2018[d]).

2.3. Direct Shear Test

A series of unconsolidated undrained (UU) direct shear tests, as specified in AS 1289.6.2.2 (1998) and commonly adopted in the literature (e.g. Qu et al. 2013; Calik and Sadoglu 2014; Al-Aqtash and Bandini 2015; Qu and Zhao 2016; Wang et al. 2017), were carried out to investigate the shear strength behavior of the soil–rubber interface. Each of the nine soil–rubber mix designs outlined in Table 2 was tested for shear strength at four different normal stresses, i.e. σ_n=100 kPa, 200 kPa, 300 kPa and 400 kPa. To minimize both drainage and excess pore–water pressure effects (thus simulating undrained soil behavior), a high shear rate of 1 mm/min was adopted for the shearing phase (Cetin et al. 2006; Sezer et al. 2006; Bai and Liu 2012). Shear stress was recorded as a function of horizontal displacement up to a total displacement of 10 mm to quantify the stress–displacement response at both peak and post–peak (or critical state) conditions. In addition, the conventional Mohr–Coulomb failure criterion (using a total stress approach) was implemented to arrive at the apparent shear strength parameters at peak condition (Bai and Liu 2012; Al-Aqtash and Bandini 2015).

3. Experimental Results and Discussion

3.1. Shear Stress–Horizontal Displacement Response

Typical shear stress–horizontal displacement curves for the natural soil and various soil–rubber composites at σ_n=200 kPa are shown in Figures 3a and 3b for Rubbers C and B, respectively. The stress–dispalcement response exhibited a rise–fall–plateau behavior with visually detectable peak points, thus signifying a strain–softening character for the tested samples. This effect, however, was less evident for samples reinforced with Rubber B, particularly at higher normal stresses as well as higher rubber inclusions (e.g. compare R_c=30% in Figures 3a and 3b). The critical shear strength τ_{cr} was defined as the minimum shear stress exhibited within the 6–9 mm horizontal displacement region, while the peak

shear strength τ_p was visually quantified for the majority of cases (Cetin et al. 2006; Liu and Evett 2009). The stress–displacement relationship at a given normal stress was dependent on both the rubber content and the rubber size, with the former portraying a more pronounced role. For both rubber types, the higher the rubber content the higher the exhibited peak and critical shear strength values. The horizontal displacement at failure $\Delta\delta_p$ was also dependent on the rubber content, and to a lesser degree the rubber size. In general, the higher the rubber content (and/or the larger the rubber size) the higher the horizontal displacement at failure, thus indicating a notable improvement in the composite's ductility. At σ_n=200 kPa, for instance, the natural soil resulted in τ_p=94.65 kPa ($\Delta\delta_p$=2.24 mm), while the inclusion of 5%, 10%, 20% and 30% Rubber C resulted in τ_p=96.48 kPa ($\Delta\delta_p$=2.71 mm), 107.01 kPa ($\Delta\delta_p$=3.34 mm), 136.23 kPa ($\Delta\delta_p$=4.21 mm) and 151.88 kPa ($\Delta\delta_p$=4.80 mm), respectively. For similar inclusions of Rubber B, these values were measured as 100.54 kPa ($\Delta\delta_p$=2.78 mm), 116.08 kPa ($\Delta\delta_p$=3.14 mm), 130.11 kPa ($\Delta\delta_p$=3.74 mm) and 139.48 kPa ($\Delta\delta_p$=7.51 mm), respectively. Similar observations have also been reported by researchers such as Tatlisoz et al. (1997), Özkul and Baykal (2006) and Signes et al. (2016).

Figures 4a and 4b illustrate the variations of the peak and critical shear strength values against normal stress for the tested samples, respectively. For rubber inclusions equal to or less than 10%, the rubber of coarser category, Rubber B, slightly outperformed the finer Rubber C in terms of higher peak shear strength values, while an opposite effect was evident for higher rubber inclusions. In this case, R_c=20% served as a transition point, manifesting a similar performance with marginal differences for the two rubber types (see R_c=20% in Figure 4a). The higher rubber inclusion of 30%, however, gave rise to notably higher peak shear strength values for the finer Rubber C (see R_c=30% in Figure 4a). These trends are largely consistent with those reported by researchers such as Cetin et al. (2006) and Soltani et al. (2018[c]). A so–called transition was not observed for the critical shear strength, which as previously discussed, can be attributed to the strain–hardening like character exhibited at high inclusions of Rubber B, thus leading to induced strength performance at critical state condition (e.g. compare R_c=30% in Figures 3a and 3b). As a result, the critical shear strength was in favor of both a higher rubber content and a larger rubber size (see Figure 4b).

3.2. Shear Strength Parameters

The conventional Mohr–Coulomb failure criterion, using a total stress approach expressed as $\tau_p=c_p+\sigma_n\tan\varphi_p$ (c_p=cohesion; and φ_p=friction angle), was implemented to quantify the apparent shear strength parameters at peak condition, and the results are summarized in Table 3. The shear strength parameters were dependent on both the rubber content and the rubber size, with the former portraying a more significant role. For rubber inclusions equal to or less than 10%, Rubber B slightly outperformed Rubber C in terms of higher c_p and φ_p values. The performance of both rubber types, particularly in terms of cohesion c_p, were on par with each other at R_c=20% (e.g. c_p=75.89 kPa and 76.06 kPa for 20% Rubbers C and B), while the higher rubber inclusion of 30% gave rise to higher c_p and φ_p values for Rubber C (e.g. c_p=98.47 kPa and 86.19 kPa for 30% Rubbers C and B). These trends are in agreement with the results reported by Cetin et al. (2006).

Accepted manuscript doi:
10.1680/jgein.18.00045

3.3. Soil–Rubber Interactions

As outlined in Section 2.1.2 (see Figures 2c and 2f), the rubber's rough surface texture promotes adhesion and/or induces frictional resistance at the soil–rubber interface, and thus alters the soil fabric into a coherent matrix of induced strength and improved ductility. As such, the interfacial shear strength of rubber–reinforced fine–grained soils is governed by the following amending mechanisms (Tang et al. 2007, 2010; Trouzine et al. 2012; Kalkan 2013; Yadav and Tiwari 2017[b]; Zhang et al. 2017; Mirzababaei et al. 2018[b], 2018[c]; Soltani et al. 2018[b], 2018[c]):

- Frictional resistance generated as a result of soil–rubber contact.
- Mechanical interlocking of rubber particles and soil grains.

The frictional resistance generated at the soil–rubber interface is primarily a function of the soil–rubber contact area, with greater contact levels promoting a more pronounced interfacial frictional resistance, and thus a higher resistance to shearing. This amending mechanism can therefore be ascribed to the rubber content, and to a lesser degree the rubber size. For a given rubber type (constant rubber size), the greater the number of included rubber particles (increase in rubber content) the greater the achieved contact level between the rubber particles and the soil grains, which in turn promotes an induced interfacial frictional resistance followed by an improved shear strength. Similarly, for a given rubber content, the rubber of coarser category is in favor of yielding a greater soil–rubber contact level, and hence a greater interfacial frictional resistance coupled with an improved shear strength. The generated frictional resistance also depends upon the magnitude of confinement (or normal stress) acting on the soil–rubber interface, and increases upon increasing the normal stress. As illustrated in Figure 4a, for instance, 20% Rubber C promoted a 38% improvement in the peak shear strength at σ_n=100 kPa (i.e. τ_p increased from 74.25 kPa 'Point A_1' to 102.61 kPa 'Point B_1'), while a greater improvement of 50% was achieved for the same rubber inclusion at σ_n=400 kPa (i.e. τ_p increased from 126.45 kPa 'Point A_2' to 189.67 kPa 'Point B_2'). As another typical case depicted in Figure 4b, 20% Rubber B promoted a 53% improvement in the critical shear strength at σ_n=100 kPa (i.e. τ_{cr} increased from 49.19 kPa 'Point A'_1' to 75.22 kPa 'Point B'_1'), whereas a greater improvement of 67% was observed for the same rubber inclusion at σ_n=400 kPa (i.e. τ_{cr} increased from 89.36 kPa 'Point A'_2' to 149.22 kPa 'Point B'_2').

The interlocking of rubber particles and soil grains, achieved during sample preparation (or compaction), induces adhesion at the soil–rubber interface by restricting the movement of soil grains (undergoing shearing) interlocked to the rubber (Mukherjee and Mishra 2017, 2018; Wang et al. 2018). Quite clearly, the more effective the mechanical interlocking the higher the resistance to shearing. Consequently, this amending mechanism is in line with the rubber content, and more importantly the rubber shape. For a given rubber type (constant rubber size and shape), the greater the number of rubber particles (increase in rubber content) present at the soil–rubber interface the greater the number of interlocked (or enwrapped) soil–rubber lumps, and thus the greater the magnitude of improvement in shear strength. As opposed to the granular form factor of the finer Rubber C (see Figure 2b), the particles of Rubber B are more fiber–shaped (see Figure 2e), thus making for a more pronounced mechanical interlocking by entwining within the soil matrix and hence immobilizing the soil grains undergoing shearing with increased efficiency.

It should be noted that both amending mechanisms described above only hold provided that the rubber particles do not adhere to each other (or cluster) during sample preparation (or compaction) and shearing (Cabalar et al. 2014; Cabalar and Karabash 2015; Yadav and

Accepted manuscript doi:
10.1680/jgein.18.00045

Tiwari et al. 2017[b]; Zhang et al. 2017). At high rubber contents and potentially for larger rubber sizes, the behavior of the composite at some points of the soil–rubber interface may be governed by a rubber–to–rubber interaction, which though offers a notable improvement to the composite's ductility (e.g. see R_c=30% in Figure 3b), offsets the desired soil–to–rubber interaction capable of improving the peak shear strength. For rubber inclusions equal to or less than 10%, the rubber of coarser category, Rubber B, slightly outperformed the finer Rubber C in terms of higher peak shear strength properties, thus indicating an induced interfacial frictional resistance and/or mechanical interlocking owing to the larger size and fibrous form factor of Rubber B. The rubber inclusion of 20% served as a transition point, manifesting a similar performance with marginal differences for the two rubber types, and thus marking the appearance of some rubber–clustering effects for the coarser rubber. For the higher rubber inclusion of 30%, the peak shear strength properties for Rubber B dropped below that of Rubber C, signifying an induced rubber–clustering effect in the presence of the coarser rubber (see Figure 4a and Table 3). Such a transition was not observed for the critical shear strength (see Figure 4b), which can be attributed to the dominant rubber–to–rubber interaction exhibited at high inclusions of Rubber B, thus prompting a strain–hardening like character coupled with induced strength performance at critical state condition compared with that of Rubber C.

4. Dimensional Analysis

4.1. Model Development

The derivation of a dimensional model accounting for all variables governing a physical problem, the shear strength phenomenon in this case, is a formidable but practice–oriented task. A practical dimensional model can be characterized as one that maintains a perfect balance between simplicity (ease of application) and accuracy, thus involving a limited number of conventional physical parameters capable of arriving at a reliable estimate of the problem in hand (Simon et al. 2017). It is therefore essential avoiding the introduction of any physical parameters which are equally (or more) difficult to measure compared with the physical problem intended to be modeled. For a given fine–grained soil reinforced with a particular type of rubber, governing variables with respect to the soil–rubber shear strength problem, as evident with the experimental results discussed in Section 3, can be categorized as: i) weight of soil solids W_s (in kg); ii) weight of rubber particles W_r (in kg); iii) weight of water W_w (in kg); iv) initial dry unit weight of the mixture composite γ_{do} (in N/m^3); v) specific surface area of the mixture S_a (in m^2/kg); vi) the rubber's mean particle size (or diameter) d_{50} (in m); and vii) normal stress σ_n (in Pa). The soil–rubber shear strength problem, for peak or critical state condition $\tau_p \vee \tau_{cr}$ (in Pa), can therefore be expressed as:

$$\tau_p \vee \tau_{cr} = f_1(W_s, W_r, W_w, \gamma_{do}, S_a, d_{50}, \sigma_n) \quad (1)$$

where f_1=an unknown multi–variable functional expression.

Although the shear strength of an unsaturated geomaterial, such as the soil–rubber composite in this study, is well known to be related to its matric suction, one may argue that an accurate measurement of suction, for fine–grained soils in particular, is a rather difficult and time–consuming task (Johari et al. 2006; Agus et al. 2010; Malaya and Sreedeep 2011). A typical undrained direct shear test (the problem in hand), however, is deemed as a routine test commonly performed in most laboratories with much less effort. To maintain model simplicity/practicality, it was therefore decided to disregard introducing suction as a governing variable. Interestingly, such a simplification complies with most of the existing literature, where various forms of empirical and dimensional models have been developed

Accepted manuscript doi:
10.1680/jgein.18.00045

and validated for different geomaterials without regarding suction as an input variable (e.g. Rao et al. 2004; Buzzi et al. 2011; Williamson and Cortes 2014; Berrah et al. 2016; Zhao et al. 2016).

The Buckingham Pi concept provides a method for deriving sets of dimensionless variables (commonly referred to as Pi or π terms) from given physical parameters, even if the governing functional expression, e.g. f_1 in Equation 1, remains unknown (Buckingham 1914). Despite the concept's successful adoption as a basic principle in fluid mechanics, its application has been less extended to geotechnical–related problems (e.g. Butterfield 1999; Buzzi 2010; Buzzi et al. 2011; Williamson and Cortes 2014; Berrah et al. 2016). The concept states that any physical problem, such as that expressed by Equation 1, involving n number of physical parameters with m number of basic physical dimensions (or units) can be further simplified to a new problem involving $k=n–m$ number of dimensionless variables (or Pi terms) capable of adequately describing the original problem in hand. Therefore, the system of $n=7$ physical parameters (γ_{do} is related to W_s and W_r) and $m=3$ basic physical dimensions (i.e. mass [M], length [L] and time [T]) given in Equation 1 can be simplified to a new system of $k=4$ dimensionless variables given as:

$$\pi_o = \frac{\tau_p \vee \tau_{cr}}{\sigma_n} \tag{2}$$

$$\pi_1 = \frac{W_r}{W_s} = R_c \tag{3}$$

$$\pi_2 = \frac{W_w}{W_s} = w_o(1+R_c) \tag{4}$$

$$\pi_3 = \frac{S_a\sqrt{\sigma_n \gamma_{do} d_{50}}}{g} \tag{5}$$

where π_o=dependent Pi term; π_1, π_2 and π_3=independent Pi terms; w_o=initial water content of the mixture composite ($=W_w/[W_s+W_r]$); and g=standard gravitational acceleration (=9.81 m/s^2).

The soil–rubber shear strength problem, for peak or critical state condition, can therefore be represented by the following simplified expression:

$$\pi_o = \frac{\tau_p \vee \tau_{cr}}{\sigma_n} = f_2(\pi_1, \pi_2, \pi_3) \tag{6}$$

As outlined in Section 2.2, samples for the direct shear tests were prepared at the corresponding optimum condition of each mixture, meaning that $w_o=w_{opt}$ and $\gamma_{do}=\gamma_{dmax}$ (see Table 2). Furthermore, the specific surface area for both the natural soil and various soil–rubber mixtures was estimated by the following empirical relationship (Locat et al. 1984; Williamson and Cortes 2014; Zhao et al. 2016):

$$I_p = 0.7(S_a - 5) \tag{7}$$

where S_a=specific surface area (in m^2/g); and I_p=plasticity index (in %), as provided in Table 2.

In Equation 6, f_2 is an unknown multi–variable functional expression, which is to be obtained through trial and error (Simon et al. 2017). To complement the derivation of a practical dimensional model, it is essential that any suggested functional expressions, while arriving at a reliable estimate of τ_p and τ_{cr}, contain a limited number of model (or fitting) parameters, which could be adequately calibrated by minimal experimental effort as well as simple explicit calculations. Although a standard ad hoc solution to f_2 is non–existent, it has been the

Accepted manuscript doi:
10.1680/jgein.18.00045

authors' experience that two inductive approaches, hereafter categorized as Methods A and B, could be employed to complement the trial and error phase, and thus arrive at suitable functional expressions:

4.1.1. Method A

The first approach, the results of which will be presented as Models M_1 and M_2 in Sections 4.3.1 and 4.3.2, relies on incorporating the existing independent Pi terms (Equations 3, 4 and 5) into a single dimensionless number, such as η, capable of adequately quantifying the dependent Pi term (Equation 2) by means of a conventional single–variable function (e.g. linear, quadratic polynomial and power). The benefit of this particular approach lies within a further simplification of the multi–variable governing problem (expressed by Equation 6) to a single–variable governing problem, thereby minimizing the number of expected model parameters as well as the associated experimental effort for their calibration. On the downside, one should consider that unification of the independent Pi terms is highly contingent, and thus depends upon a rigorous trial and error to be carried out which becomes increasingly difficult, if not impossible, when dealing with a large number of independent Pi terms. Provided that the three independent Pi terms given in Equation 6 could be effectively incorporated into a single dimensionless number, the soil–rubber shear strength problem can be expressed in terms of a single governing variable as:

$$\pi_o = f_2(\pi_1, \pi_2, \pi_3) = f_3(\eta) \tag{8}$$

where f_3=a conventional single–variable function; and η=a dimensionless number yielded by incorporating the independent Pi terms through trial and error.

4.1.2. Method B

The second approach, the results of which will be presented as Model M_3 in Section 4.3.3, involves a step–by–step examination of conventional multi–variable functions to arrive at the most simple functional expression capable of quantifying the dependent Pi term with an acceptable degree of accuracy. In essence, such a procedure resembles a typical multiple regression analysis, and thus to some extent prevails the contingent issue associated with Method A. However, as with any multiple regression analysis, the greater the number of input variables (or independent Pi terms) the greater the number of model parameters (or regression coefficients), and thus the more experimental measurements required for model calibration. In this context, two common yet simple solutions include the multi–variable linear and power functions, which for the three independent Pi terms problem given in Equation 6 can be expressed as:

$$\pi_o = f_2(\pi_1, \pi_2, \pi_3) = \beta_o + \sum_{j=1}^{3} \beta_j \pi_j \tag{9}$$

$$\pi_o = f_2(\pi_1, \pi_2, \pi_3) = \prod_{j=1}^{3} \pi_j^{\beta_{j-1}} \tag{10}$$

where β_o, β_j and β_{j-1}=model parameters (dimensionless); and j=index of summation or multiplication.

4.2. Model Validation

In the present study, a total of three dimensional models, two representing Method A (see Models M_1 and M_2 in Sections 4.3.1 and 4.3.2) and one representing Method B (see Model M_3 in Section 4.3.3), were proposed. Each model was fitted to the experimental τ_p and τ_{cr} datasets (see Table A1 in Appendix A in Supplemental Materials) by means of the least squares optimization technique (Soltani et al. 2018[e]). Statistical fit–measure indices, namely the coefficient of determination R^2 (dimensionless), the root mean squares error RMSE (in kPa) and the mean absolute percentage error MAPE (in %), were then obtained for model validation (and to compare the performance of the proposed models) by the following relationships (Estabragh et al. 2016):

$$\mathrm{RMSE} = \sqrt{\frac{1}{N}\sum_{i=1}^{N}(y_{mi} - y_{ai})^2} \tag{11}$$

$$\mathrm{MAPE} = \frac{1}{N}\sum_{i=1}^{N}\left|\frac{y_{mi} - y_{ai}}{y_{ai}}\right| \times 100 \tag{12}$$

where y_m=predicted (or modeled) value of the dependent variable y (=$\tau_p \vee \tau_{cr}$); y_a=actual value of the dependent variable y (presented in Table A1 of Appendix A in Supplemental Materials); i=index of summation; and N=number of data points used for model development (=20 for each rubber type consisting of 4 unreinforced and 16 reinforced, as shown in Table A1 of Appendix A in Supplemental Materials).

4.3. Proposed Dimensional Models

4.3.1. Model M_1

Through trial and error, the three independent Pi terms (Equations 3, 4 and 5) were incorporated into a single dimensionless number, hereafter denoted as the first dimensionless shear number η_1, which can be given as:

$$\eta_1 = \frac{10^8 \pi_2}{(1-\pi_1)\pi_3} = \frac{10^8 g w_o (1+R_c)}{S_a (1-R_c)\sqrt{\sigma_n \gamma_{do} d_{50}}} \tag{13}$$

Figures 5a and 5b illustrate the variations of π_o (Equation 2) against η_1 (Equation 13) at both peak and critical state conditions for Rubbers C and B, respectively. As depicted in the figures, a rather strong correlation in the form of a conventional single–variable linear function, i.e. $y=y_o+ax$, can be obtained between π_o and η_1. Let $\pi_o=\beta_o+\beta_1\eta_1$, one can therefore derive the following for $\tau_p \vee \tau_{cr}$:

$$\tau_p \vee \tau_{cr} = \sigma_n(\beta_o + \beta_1\eta_1) \tag{14}$$

where β_o and β_1=model parameters (dimensionless).

The regression analysis outputs with respect to the proposed dimensional model M_1 (Equation 14) are summarized in Table 4 for both rubber types. The high R^2 and low MAPE (and RMSE) values imply a strong agreement between actual and predicted shear strength data, both in terms of correlation and error. The R^2 values mainly surpassed the 0.95 margin, indicating that leastwise 95% of the variations in experimental observations are captured and further explained by Model M_1. The MAPE values were found to be less than 7% for all cases, signifying a maximum offset of 7% associated with the predictions.

Figures 6a and 6b illustrate predicted (by Model M_1 or Equation 14) versus actual data, along with the corresponding 95% prediction bands/intervals, for various soil–rubber composites at peak and critical state conditions, respectively. Although some scatter can be observed,

Accepted manuscript doi:
10.1680/jgein.18.00045

nearly all data points lie between the upper and lower 95% prediction intervals, thus indicating no major outliers associated with the predictions. The coefficient of determination was also obtained for these combined datasets, which resulted in a net R^2 of 0.950 and 0.979 for τ_p and τ_{cr}, respectively.

The proposed dimensional model M_1 (Equation 14) contains two model parameters, i.e. β_o and β_1, which can be calibrated by minimal experimental effort, and thus further implemented for predictive purposes. The model parameters can be adequately estimated by a total of two direct shear tests. Two test scenarios consisting of the natural soil and a desired soil–rubber mixture, each at a median normal stress, are recommended for the calibration phase. Although the choice of rubber content for the soil–rubber mixture is arbitrary, from a statistical perspective, a median rubber content is expected to yield a more reliable estimate of the model parameters (Mirzababaei et al. 2018[a]). Consider the following designations:

- $\eta_1^{(R_c^o,\sigma_n^m)}$ =first dimensionless shear number (Equation 13) for no rubber inclusion, i.e. R_c^o, at a median normal stress, i.e. σ_n^m.
- $\tau_p^{(R_c^o,\sigma_n^m)} \vee \tau_{cr}^{(R_c^o,\sigma_n^m)}$ =actual peak or critical shear strength for no rubber inclusion, i.e. R_c^o, at a median normal stress, i.e. σ_n^m.
- $\eta_1^{(R_c^m,\sigma_n^m)}$ =first dimensionless shear number (Equation 13) for a median rubber content, i.e. R_c^m, at a median normal stress, i.e. σ_n^m.
- $\tau_p^{(R_c^m,\sigma_n^m)} \vee \tau_{cr}^{(R_c^m,\sigma_n^m)}$ =actual peak or critical shear strength for a median rubber content, i.e. R_c^m, at a median normal stress, i.e. σ_n^m.

Therefore, the following system of two linear equations should be solved to arrive at an estimate of the M_1 model parameters β_o and β_1:

$$M_1: \begin{cases} \dfrac{\tau_p^{(R_c^o,\sigma_n^m)} \vee \tau_{cr}^{(R_c^o,\sigma_n^m)}}{\sigma_n^m} = \beta_o + \beta_1 \eta_1^{(R_c^o,\sigma_n^m)} \\ \dfrac{\tau_p^{(R_c^m,\sigma_n^m)} \vee \tau_{cr}^{(R_c^m,\sigma_n^m)}}{\sigma_n^m} = \beta_o + \beta_1 \eta_1^{(R_c^m,\sigma_n^m)} \end{cases} \quad (15)$$

An explicit solution to Equation 15 is provided in Equation B4 of Appendix B.

4.3.2. Model M_2

Through trial and error, a second dimensionless shear number, hereafter denoted as η_2, was suggested as:

$$\eta_2 = \frac{(1-\pi_1)\pi_2\pi_3}{10^6} = \frac{S_a w_o (1-R_c^2)\sqrt{\sigma_n \gamma_{do} d_{50}}}{10^6 g} \quad (16)$$

The variations of π_o (Equation 2) were plotted against the second dimensionless shear number η_2 (Equation 16), and the results are provided in Figures 7a and 7b at both peak and critical state conditions for Rubbers C and B, respectively. In this case, a rather strong correlation in the form of a conventional single–variable power function, i.e. $y=ax^b$, was observed between π_o and η_2. Let $\pi_o=\beta_o\eta_2^{\beta_1}$, the following can therefore be written for $\tau_p \vee \tau_{cr}$:

$$\tau_p \vee \tau_{cr} = \sigma_n \beta_o \eta_2^{\beta_1} \quad (17)$$

where β_o and β_1=model parameters (dimensionless).

Accepted manuscript doi:
10.1680/jgein.18.00045

The regression analysis outputs with respect to the proposed dimensional model M_2 (Equation 17) are summarized in Table 5 for both rubber types. Model M_2 mainly exhibited similar R^2, RMSE and MAPE values compared with that of Model M_1 (Equation 14), thus indicating a similar performance for both models. Similar to Model M_1, the R^2 values were mainly greater than 0.95, while the MAPE values were found to be less than 7% for all cases. Figures 8a and 8b illustrate predicted (by Model M_2 or Equation 17) versus actual data, along with the corresponding 95% prediction bands/intervals, for various soil–rubber composites at peak and critical state conditions, respectively. Similar to Model M_1, some scatter can still be observed; however, nearly all data points position themselves between the upper and lower 95% prediction intervals, thus indicating no particular outliers associated with the predictions. The coefficient of determination for these combined datasets were obtained as 0.955 for τ_p and 0.976 for τ_{cr}, which are similar to those obtained for Model M_1.

The calibration procedure for Model M_2 (Equation 17), as a two parameter model, would essentially be similar to that described for Model M_1. In this case, however, the non–linear character of Model M_2, represented by the power component β_1, should first be linearized by means of a logarithmic transformation. Upon linearization, the following system of two semi–linear equations should be solved to arrive at an estimate of the M_2 model parameters β_o and β_1:

$$\mathrm{M}_2 : \begin{cases} \mathrm{Ln}\left\langle \dfrac{\tau_{\mathrm{p}}^{(R_{\mathrm{c}}^{\mathrm{o}},\sigma_{\mathrm{n}}^{\mathrm{m}})} \vee \tau_{\mathrm{cr}}^{(R_{\mathrm{c}}^{\mathrm{o}},\sigma_{\mathrm{n}}^{\mathrm{m}})}}{\sigma_{\mathrm{n}}^{\mathrm{m}}} \right\rangle = \mathrm{Ln}\left\langle \beta_{\mathrm{o}} \right\rangle + \beta_1 \mathrm{Ln}\left\langle \eta_2^{(R_{\mathrm{c}}^{\mathrm{o}},\sigma_{\mathrm{n}}^{\mathrm{m}})} \right\rangle \\ \mathrm{Ln}\left\langle \dfrac{\tau_{\mathrm{p}}^{(R_{\mathrm{c}}^{\mathrm{m}},\sigma_{\mathrm{n}}^{\mathrm{m}})} \vee \tau_{\mathrm{cr}}^{(R_{\mathrm{c}}^{\mathrm{m}},\sigma_{\mathrm{n}}^{\mathrm{m}})}}{\sigma_{\mathrm{n}}^{\mathrm{m}}} \right\rangle = \mathrm{Ln}\left\langle \beta_{\mathrm{o}} \right\rangle + \beta_1 \mathrm{Ln}\left\langle \eta_2^{(R_{\mathrm{c}}^{\mathrm{m}},\sigma_{\mathrm{n}}^{\mathrm{m}})} \right\rangle \end{cases} \tag{18}$$

An explicit solution to Equation 18 is provided in Equation B5 of Appendix B in Supplemental Materials. The explicit solution to the M_2 model parameters is of slightly greater complexity compared with that of Model M_1 (compare Equations B4 and B5 in Appendix B in Supplemental Materials). As it stands, Model M_1 offers a more practical calibration procedure, while maintaining the same performance offered by the more complex Model M_2.

4.3.3. Model M_3

Upon examining various forms of conventional multi–variable functions, a modified form of the three–variable power function, similar to that given in Equation 10, was selected as the governing functional expression to link the three independent Pi terms (Equations 3, 4 and 5) to the dependent Pi term (Equation 2), which can be given as:

$$\pi_{\mathrm{o}} = (1-\pi_1)^{\beta_{\mathrm{o}}} \pi_2^{\beta_1} \left(\frac{\pi_3}{10^6}\right)^{\beta_2} = (1-R_{\mathrm{c}})^{\beta_{\mathrm{o}}} \left[w_{\mathrm{o}}(1+R_{\mathrm{c}})\right]^{\beta_1} \left(\frac{S_{\mathrm{a}}\sqrt{\sigma_{\mathrm{n}}\gamma_{\mathrm{do}}d_{50}}}{10^6\,\mathrm{g}}\right)^{\beta_2} \tag{19}$$

Provided that Equation 19 holds, equating Equations 2 and 19 yields the following for $\tau_p \vee \tau_{cr}$:

$$\tau_{\mathrm{p}} \vee \tau_{\mathrm{cr}} = \sigma_{\mathrm{n}}(1-R_{\mathrm{c}})^{\beta_{\mathrm{o}}} \left[w_{\mathrm{o}}(1+R_{\mathrm{c}})\right]^{\beta_1} \left(\frac{S_{\mathrm{a}}\sqrt{\sigma_{\mathrm{n}}\gamma_{\mathrm{do}}d_{50}}}{10^6\,\mathrm{g}}\right)^{\beta_2} \tag{20}$$

where β_o, β_1 and β_2=model parameters (dimensionless).

Figures 9a and 9b illustrate the variations of both predicted (by Model M_3 or Equation 20) and actual τ_p and τ_{cr} data against normal stress for Rubbers C and B, respectively. The

Accepted manuscript doi:
10.1680/jgein.18.00045

proposed dimensional model M_3 well correlates with the experimental observations, as evident with the clustering of predicted and actual data in the figures. Most of the predicted values perfectly overlap with their actual counterparts, thus indicating an excellent capacity to simulate the shear strength response at both peak and critical state conditions.

The regression analysis outputs with respect to the proposed dimensional model M_3 (Equation 20) are summarized in Table 6 for both rubber types. Model M_3 outperformed both Models M_1 (Equation 14) and M_2 (Equation 17), as evident with the higher R^2 and lower RMSE and MAPE values. The R^2 values were unanimously above the 0.98 margin, indicating an excellent goodness of fit. The MAPE values were less the 5% for all cases, thus manifesting a 2% improvement compared with that observed for Models M_1 and M_2.

Figures 10a and 10b illustrate predicted (by Model M_3 or Equation 20) versus actual data, along with the corresponding 95% prediction bands/intervals, for various soil–rubber composites at peak and critical state conditions, respectively. In comparison to Models M_1 and M_2, the data points lie closer to the line of equality, i.e. $y=x$, thus manifesting minimal scatter and no particular outliers associated with the predictions. The coefficient of determination for these combined datasets were obtained as 0.961 and 0.978 for τ_p and τ_{cr}, respectively.

The proposed dimensional model M_3 (Equation 20) is a three parameter model, thus a total of three direct shear tests would be required for its calibration. The suggested test scenarios can be given as:

- The natural soil (or no rubber inclusion), i.e. R_c^o, at a low normal stress, i.e. σ_n^o.
- The natural soil (or no rubber inclusion), i.e. R_c^o, at a high normal stress, i.e. σ_n^∞.
- A desired soil–rubber mixture (preferably with a median rubber content, i.e. R_c^m) at a median normal stress, i.e. σ_n^m.

Similar to that described for Model M_2 (Equation 17), the non–linear character of Model M_3, represented by the power components β_o, β_1 and β_2, should first be linearized by means of a logarithmic transformation. Upon linearization, the following system of three semi–linear equations should be solved to arrive at an estimate of the M_3 model parameters β_o, β_1 and β_2:

$$\mathrm{M}_3:\begin{cases}\mathrm{Ln}\left\langle\dfrac{\tau_p^{(R_c^o,\sigma_n^o)}\vee\tau_{cr}^{(R_c^o,\sigma_n^o)}}{\sigma_n^o}\right\rangle=\beta_o\mathrm{Ln}\left\langle 1-\pi_1^{(R_c^o,\sigma_n^o)}\right\rangle+\beta_1\mathrm{Ln}\left\langle\pi_2^{(R_c^o,\sigma_n^o)}\right\rangle+\beta_2\mathrm{Ln}\left\langle\dfrac{\pi_3^{(R_c^o,\sigma_n^o)}}{10^6}\right\rangle\\ \mathrm{Ln}\left\langle\dfrac{\tau_p^{(R_c^o,\sigma_n^\infty)}\vee\tau_{cr}^{(R_c^o,\sigma_n^\infty)}}{\sigma_n^\infty}\right\rangle=\beta_o\mathrm{Ln}\left\langle 1-\pi_1^{(R_c^o,\sigma_n^\infty)}\right\rangle+\beta_1\mathrm{Ln}\left\langle\pi_2^{(R_c^o,\sigma_n^\infty)}\right\rangle+\beta_2\mathrm{Ln}\left\langle\dfrac{\pi_3^{(R_c^o,\sigma_n^\infty)}}{10^6}\right\rangle\\ \mathrm{Ln}\left\langle\dfrac{\tau_p^{(R_c^m,\sigma_n^m)}\vee\tau_{cr}^{(R_c^m,\sigma_n^m)}}{\sigma_n^m}\right\rangle=\beta_o\mathrm{Ln}\left\langle 1-\pi_1^{(R_c^m,\sigma_n^m)}\right\rangle+\beta_1\mathrm{Ln}\left\langle\pi_2^{(R_c^m,\sigma_n^m)}\right\rangle+\beta_2\mathrm{Ln}\left\langle\dfrac{\pi_3^{(R_c^m,\sigma_n^m)}}{10^6}\right\rangle\end{cases}\qquad(21)$$

An explicit solution to Equation 21 is provided in Equation B6 of Appendix B in Supplemental Materials. Quite clearly, the explicit solution to the M_3 model parameters is of significant complexity compared with that of Models M_1 and M_2 (compare Equation B6 with Equations B4 and B5 in Appendix B in Supplemental Materials). In essence, Model M_3 sacrifices simplicity/practicality in favor of a higher accuracy.

Accepted manuscript doi:
10.1680/jgein.18.00045

4.4. Modelling the Shear Stress–Horizonal Displacement Locus

As evident with the results presented in the previous section, the proposed dimensional models, Model M_3 in particular, well predict the shear strength response of the soil–rubber composite at both peak and critical state conditions. It was therefore perceived that the same models, if rewritten in terms of shear stress as a function of horizontal displacement, could potentially provide a basis for simulating the shear stress–horizontal displacement locus during shear evolvement. Let Model M_3 (Equation 20), the most superior dimensional model as evident with the results outlined in Section 4.3.3, be rewritten in terms of horizontal displacement as:

$$\tau(\Delta\delta) = \sigma_n (1 - R_c)^{\beta_o(\Delta\delta)} \left[w_o (1 + R_c) \right]^{\beta_1(\Delta\delta)} \left(\frac{S_a \sqrt{\sigma_n \gamma_{do} d_{50}}}{10^6 g} \right)^{\beta_2(\Delta\delta)} \quad (22)$$

where $\tau(\Delta\delta)$=shear stress with respect to horizontal displacement $\Delta\delta$ (in Pa); and $\beta_o(\Delta\delta)$, $\beta_1(\Delta\delta)$ and $\beta_2(\Delta\delta)$=model parameters (dimensionless), which are a function of horizontal displacement $\Delta\delta$.

Provided that Equation 22 holds, one can therefore arrive at an estimate of the shear stress for any given horizontal displacement, and thus construct the corresponding shear stress–horizontal displacement curve. As opposed to continuous mathematical functions, such as hyperbolic–based functions (e.g. Kondner 1963; Duncan and Chang 1970; Stark et al. 1994; Horpibulsuk and Miura 2001; Horpibulsuk and Rachan 2004), which simulate the shear stress–horizontal displacement response by enforcing a predefined form factor over a continues horizontal displacement domain, the dimensional model given in Equation 22 is a discrete function in nature, and thus simulates each shear stress–horizontal displacement curve point independently. As such, a predefined form factor is not enforced to the problem in hand, thereby allowing for indigenous material properties such as strain–softening to be simply quantified with more accuracy. It has been the authors' experience that a total of six arbitrary horizontal displacement values would satisfy the construction of a desired shear stress–horizontal displacement curve. Quite clearly, the greater the number of adopted horizontal displacement values the more realistic the constructed curve. To test the proposed hypothesis, the performance of the proposed dimensional model given in Equation 22 was examined at six different low to high horizontal displacements, i.e. $\Delta\delta$=0.5 mm, 1 mm, 2 mm, 4 mm, 6 mm and 8 mm, and the results are provided in Figure 11 for both rubber types. An obvious clustering of predicted and actual data can be observed, with most of the predicted values perfectly overlapping with their actual counterparts, thus confirming the model's capacity to capture the shear stress response with respect to horizontal displacement.

Figure 12 illustrates typical experimental shear stress–horizontal displacement curves along with their respective simulations by means of the proposed dimensional model given in Equation 22. The constructed curves perfectly overlap with their actual counterparts. In particular, the strain–softening character is well simulated by the proposed model, thus resolving an inherent issue associated with common continuous simulative functions. The calibration procedure for Equation 22 would be identical to that described for Model M_3 (Equation 20) in Section 4.3.3. In this case, however, for each adopted horizontal displacement $\Delta\delta$, a separate system of three semi–linear equations should to be solved to arrive at an estimate of the corresponding model parameters $\beta_o(\Delta\delta)$, $\beta_1(\Delta\delta)$ and $\beta_2(\Delta\delta)$.

Accepted manuscript doi:
10.1680/jgein.18.00045

5. Conclusions

The following conclusions can be drawn from this study:

- The rubber inclusions altered the soil fabric into a coherent matrix of induced strength and improved ductility through amendments achieved in two aspects: i) frictional resistance generated as a result of soil–rubber contact; and ii) mechanical interlocking of rubber particles and soil grains. Provided that the rubber particles do not cluster during compaction and shearing, both amending mechanisms are expected to be in favor of a higher rubber content, and to a lesser degree a larger rubber size.
- The shear stress–horizontal dispalcement response exhibited a strain–softening character for both the natural soil and various soil–rubber composites. This effect, however, was less evident for samples reinforced with high inclusions (particularly R_c=30%) of the coarser rubber. This behavior was attributed to the dominant rubber–to–rubber interaction (or rubber–clustering) exhibited at high inclusions of the coarser rubber.
- For $R_c \leq 10\%$, the rubber of coarser category, Rubber B, slightly outperformed the finer Rubber C in terms of higher peak shear strength properties. R_c=20% served as a transition point, manifesting a similar performance with marginal differences for the two rubber types. At R_c=30%, the peak shear strength properties for Rubber B dropped below that of Rubber C, signifying an induced rubber–clustering effect in the presence of the coarser rubber. Such a transition was not observed for the critical shear strength values, which was attributed to the strain–hardening like character exhibited at high inclusions of Rubber B.
- The dimensional analysis concept was extended to the soil–rubber shear strength problem, thereby leading to the development of a series of simple and practical dimensional models capable of simulating the shear stress–horizontal displacement response as a function of the composite's basic index properties. The predictive capacity of the proposed models was examined and validated by statistical techniques. The proposed dimensional models contain a limited number of fitting parameters, which can be calibrated by minimal experimental effort and hence implemented for predictive purposes.

Acknowledgements

This research was funded by the Australian Research Council (ARC) by way of project No. DP140103004; this support is gratefully acknowledged.

Accepted manuscript doi:
10.1680/jgein.18.00045

Notation

Basic SI units are given in parentheses.

C_c coefficient of curvature (dimensionless)
c_p cohesion at peak condition (Pa)
C_u coefficient of uniformity (dimensionless)
d_{10} particle diameter corresponding to 10% finer (m)
d_{30} particle diameter corresponding to 30% finer (m)
d_{50} particle diameter corresponding to 50% finer (m)
d_{60} particle diameter corresponding to 60% finer (m)
FSR free swell ratio (dimensionless)
g standard gravitational acceleration (m/s^2)
I_p plasticity index (dimensionless)
MAPE mean absolute percentage error (%)
R^2 coefficient of determination (dimensionless)
R_c rubber content (dimensionless
RMSE root mean squares error (Pa)
S_a specific surface area (m^2/kg)
w_L liquid limit (dimensionless)
w_o initial water content (dimensionless)
w_{opt} optimum water content (dimensionless)
w_P plastic limit (dimensionless)
W_r weight of rubber particles (kg)
W_s weight of soil solids (kg)
W_w weight of water (kg)
β_o, β_1 and β_2 model/fitting parameters of the dimensional models (dimensionless)
γ_{dmax} maximum dry unit weight (N/m^3)
γ_{do} initial dry unit weight (N/m^3)
$\Delta\delta_p$ horizontal displacement at failure (m)
η_1 first dimensionless shear number (dimensionless)
η_2 second dimensionless shear number (dimensionless)
π_1, π_2 and π_3 independent Pi terms (dimensionless)
π_o dependent Pi term (dimensionless)
σ_n normal stress (Pa)
$\tau(\Delta\delta)$ shear stress with respect to horizontal displacement $\Delta\delta$ (Pa)
τ_{cr} critical shear strength (Pa)
τ_p peak shear strength (Pa)
φ_p friction angle at peak condition (^{o})

Abbreviations

CH clay with high plasticity
USCS unified soil classification system
UU unconsolidated undrained

References

Agus, S. S., Schanz, T. & Fredlund, D. G. (2010). Measurements of suction versus water content for bentonite–sand mixtures. *Canadian Geotechnical Journal*, 47, No. 5, 583–594, http://dx.doi.org/10.1139/t09-120.

Al-Aqtash, U. & Bandini, P. (2015). Prediction of unsaturated shear strength of an adobe soil from the soil–water characteristic curve. *Construction and Building Materials*, 98, 892–899, http://dx.doi.org/10.1016/j.conbuildmat.2015.07.188.

Arulrajah, A., Mohammadinia, A., D'Amico, A. & Horpibulsuk, S. (2017). Effect of lime kiln dust as an alternative binder in the stabilization of construction and demolition materials. *Construction and Building Materials*, 152, No. 999–1007, http://dx.doi.org/10.1016/j.conbuildmat.2017.07.070.

AS 1289.3.2.1:09 (2009). Methods of testing soils for engineering purposes: Soil classification tests – Determination of the plastic limit of a soil. *Standards Australia*, Sydney, New South Wales, Australia.

AS 1289.3.3.1:09 (2009). Methods of testing soils for engineering purposes: Soil classification tests – Calculation of the plasticity index of a soil. *Standards Australia*, Sydney, New South Wales, Australia.

AS 1289.3.4.1:08 (2008). Methods of testing soils for engineering purposes: Soil classification tests – Determination of the linear shrinkage of a soil. *Standards Australia*, Sydney, New South Wales, Australia.

AS 1289.3.9.1:15 (2015). Methods of testing soils for engineering purposes: Soil classification tests – Determination of the cone liquid limit of a soil. *Standards Australia*, Sydney, New South Wales, Australia.

AS 1289.6.2.2:98 (1998). Methods of testing soils for engineering purposes: Soil strength and consolidation tests – determination of the shear strength of a soil – direct shear test using a shear box. *Standards Australia*, Sydney, New South Wales, Australia.

ASTM D2487-11 (2011). Standard practice for classification of soils for engineering purposes (Unified Soil Classification System). *ASTM International*, West Conshohocken, Pennsylvania, USA, http://dx.doi.org/10.1520/d2487-11.

ASTM D422-63(2007)e2 (2007). Standard test method for particle–size analysis of soils. *ASTM International*, West Conshohocken, Pennsylvania, USA, http://dx.doi.org/10.1520/d0422-63r07e02.

ASTM D698-12e2 (2012). Standard test methods for laboratory compaction characteristics of soil using standard effort (12,400 ft–lbf/ft^3 (600 kN–m/m^3)). *ASTM International*, West Conshohocken, Pennsylvania, USA, http://dx.doi.org/10.1520/d0698-12e02.

ASTM D854-14 (2014). Standard test methods for specific gravity of soil solids by water pycnometer. *ASTM International*, West Conshohocken, Pennsylvania, USA, http://dx.doi.org/10.1520/d0854-14.

Bai, F. Q. & Liu, S. H. (2012). Measurement of the shear strength of an expansive soil by combining a filter paper method and direct shear tests. *Geotechnical Testing Journal*, 35, No. 3, 451–459, http://dx.doi.org/10.1520/gtj103342.

Berrah, Y., Boumezbeur, A., Kherici, N. & Charef, N. (2016). Application of dimensional analysis and regression tools to estimate swell pressure of expansive soil in Tebessa (Algeria). *Bulletin of Engineering Geology and the Environment*, in press, http://dx.doi.org/10.1007/s10064-016-0973-4.

Briga-Sá, A., Nascimento, D., Teixeira, N., Pinto, J., Caldeira, F., Varum, H. & Paiva, A. (2013). Textile waste as an alternative thermal insulation building material solution.

Construction and Building Materials, 38, 155–160, http://dx.doi.org/10.1016/j.conbuildmat.2012.08.037.

Buckingham, E. (1914). On physically similar systems; illustrations of the use of dimensional equations. *Physical Review*, 4, No. 4, 345–376, http://dx.doi.org/10.1103/physrev.4.345.

Butterfield, R. (1999). Dimensional analysis for geotechnical engineers. *Géotechnique*, 49, No. 3, 357–366, http://dx.doi.org/10.1680/geot.1999.49.3.357.

Buzzi, O. (2010). On the use of dimensional analysis to predict swelling strain. *Engineering Geology*, 116, No. 1–2, 149–156, http://dx.doi.org/10.1016/j.enggeo.2010.08.005.

Buzzi, O., Giacomini, A. & Fityus, S. (2011). Towards a dimensionless description of soil swelling behaviour. *Géotechnique*, 61, No. 3, 271–277, http://dx.doi.org/10.1680/geot.7.00194.

Cabalar, A. F. & Karabash, Z. (2015). California bearing ratio of a sub–base material modified with tire buffings and cement addition. *Journal of Testing and Evaluation*, 43, No. 6, 1279–1287, http://dx.doi.org/10.1520/jte20130070.

Cabalar, A. F., Karabash, Z. & Mustafa, W. S. (2014) Stabilising a clay using tyre buffings and lime. *Road Materials and Pavement Design*, 15, No. 4, 872–891, http://dx.doi.org/10.1080/14680629.2014.939697.

Calik, U. & Sadoglu, E. (2014). Classification, shear strength, and durability of expansive clayey soil stabilized with lime and perlite. *Natural Hazards*, 71, No. 3, 1289–1303, http://dx.doi.org/10.1007/s11069-013-0950-1.

Cetin, H., Fener, M. & Gunaydin, O. (2006). Geotechnical properties of tire–cohesive clayey soil mixtures as a fill material. *Engineering Geology*, 88, No. 1–2, 110–120, http://dx.doi.org/10.1016/j.enggeo.2006.09.002.

Duncan, J. M. & Chang, C. Y. (1970). Nonlinear analysis of stress and strain in soils. *Journal of the Soil Mechanics and Foundations Division*, 96, No. 5, 1629–1653.

Edil, T. & Bosscher, P. (1994). Engineering properties of tire chips and soil mixtures. *Geotechnical Testing Journal*, 17, No. 4, 453–464, http://dx.doi.org/10.1520/gtj10306J.

Edincliler, A., Cabalar, A. F. & Cevik, A. (2013) Modelling dynamic behaviour of sand–waste tires mixtures using Neural Networks and Neuro–Fuzzy. *European Journal of Environmental and Civil Engineering*, 17, No. 8, 720–741, http://dx.doi.org/10.1080/19648189.2013.814552.

Edincliler, A., Cabalar, A. F., Cagatay, A. & Cevik, A. (2012) Triaxial compression behavior of sand and tire wastes using neural networks. *Neural Computing and Applications*, 21, No. 3, 441–452, http://dx.doi.org/10.1007/s00521-010-0430-4.

Estabragh, A. R., Soltani, A. & Javadi, A. A. (2016). Models for predicting the seepage velocity and seepage force in a fiber reinforced silty soil. *Computers and Geotechnics*, 75, 174–181, http://dx.doi.org/10.1016/j.compgeo.2016.02.002.

Estabragh, A. R., Soltani, A. & Javadi, A. A. (2018). Effect of pore water chemistry on the behaviour of a kaolin–bentonite mixture during drying and wetting cycles. *European Journal of Environmental and Civil Engineering*, in press, http://dx.doi.org/10.1080/19648189.2018.1428691.

Hannam, P. (2014). Tyre industry divided over how to handle toxic waste. *The Sydney Morning Herald*, Sydney, New South Wales, Australia. See http://www.smh.com.au/environment/tyre-industry-divided-over-how-to-handle-toxic-waste-20140120-314ic.html (accessed 1/29/2018)

Horpibulsuk, S. & Miura, N. (2001). Modified hyperbolic stress–strain response: Uncemented and cement stabilized clays. *Reports of the Faculty of Science and Engineering, Saga University*, 30, No. 1, 39–47.

Horpibulsuk, S. & Rachan, R. (2004). Modified hyperbolic model for capturing undrained shear behavior. *Lowland Technology International*, 6, No. 2, 11–20.

Hoy, M., Rachan, R., Horpibulsuk, S., Arulrajah, A. & Mirzababaei, M. (2017). Effect of wetting–drying cycles on compressive strength and microstructure of recycled asphalt pavement–Fly ash geopolymer. *Construction and Building Materials*, 144, 624–634, http://dx.doi.org/10.1016/j.conbuildmat.2017.03.243.

Huggins, E. & Ravichandran, N. (2011). Numerical study on the dynamic behavior of retaining walls backfilled with shredded tires. In: *GeoRisk 2011: Geotechnical Risk Assessment and Management (GSP 224)*, Juang, C. H., Phoon, K. K., Puppala, A. J., Green, R. A. & Fenton, G. A., Eds., ASCE, Atlanta, Georgia, USA, pp. 955–962, http://dx.doi.org/10.1061/41183(418)103.

Johari, A., Habibagahi, G. & Ghahramani, A. (2006). Prediction of soil–water characteristic curve using genetic programming. *Journal of Geotechnical and Geoenvironmental Engineering*, 132, No. 5, 661–665, http://dx.doi.org/10.1061/(asce)1090-0241(2006)132:5(661).

Kalkan, E. (2013). Preparation of scrap tire rubber fiber–silica fume mixtures for modification of clayey soils. *Applied Clay Science*, 80–81, 117–125, http://dx.doi.org/10.1016/j.clay.2013.06.014.

Kim, Y. T., Kim, H. J. & Lee, G. H. (2008). Mechanical behavior of lightweight soil reinforced with waste fishing net. *Geotextiles and Geomembranes*, 26, No. 6, 512–518, http://dx.doi.org/10.1016/j.geotexmem.2008.05.004.

Kondner, R. L. (1963). Hyperbolic stress–strain response: Cohesive soils. *Journal of the Soil Mechanics and Foundations Division*, 89, No. 1, 115–144.

Kua, T. A., Arulrajah, A., Mohammadinia, A., Horpibulsuk, S. & Mirzababaei, M. (2017). Stiffness and deformation properties of spent coffee grounds based geopolymers. *Construction and Building Materials*, 138, 79–87, http://dx.doi.org/10.1016/j.conbuildmat.2017.01.082.

Lee, C., Shin, H. & Lee, J. S. (2014). Behavior of sand–rubber particle mixtures: Experimental observations and numerical simulations. *International Journal for Numerical and Analytical Methods in Geomechanics*, 38, No. 16, 1651–1663, http://dx.doi.org/10.1002/nag.2264.

Li, L., Xiao, H., Ferreira, P. & Cui, X. (2016). Study of a small scale tyre–reinforced embankment. *Geotextiles and Geomembranes*, 44, No. 2, 201–208, http://dx.doi.org/10.1016/j.geotexmem.2015.08.004.

Liu, C. & Evett, J. (2009). Soil Properties: Testing, Measurement, and Evaluation (6th Ed.). Pearson/Prentice Hall, Upper Saddle River, New Jersey, USA. ISBN: 9780136141235.

Locat, J., Lefebvre, G. & Ballivy, G. (1984). Mineralogy, chemistry, and physical properties interrelationships of some sensitive clays from Eastern Canada. *Canadian Geotechnical Journal*, 21, No. 3, 530–540, http://dx.doi.org/10.1139/t84-055.

Malaya, C. & Sreedeep, S. (2011). A laboratory procedure for measuring high soil suction. *Geotechnical Testing Journal*, 34, No. 5, 396–405, http://dx.doi.org/10.1520/gtj103613.

Mirzababaei, M., Arulrajah, A., Haque, A., Nimbalkar, S. & Mohajerani, A. (2018[c]) Effect of fiber reinforcement on shear strength and void ratio of soft clay. *Geosynthetics International*, in press, http://dx.doi.org/10.1680/jgein.18.00023.

Mirzababaei, M., Arulrajah, A., Horpibulsuk, S., Soltani, A. & Khayat, N. (2018[b]) Stabilization of soft clay using short fibers and poly vinyl alcohol. *Geotextiles and Geomembranes*, 46, No. 5, 646–655, http://dx.doi.org/10.1016/j.geotexmem.2018.05.001.

Mirzababaei, M., Miraftab, M., Mohamed, M. & McMahon, P. (2013[a]). Unconfined compression strength of reinforced clays with carpet waste fibers. *Journal of Geotechnical and Geoenvironmental Engineering*, 139, No. 3, 483–493, http://dx.doi.org/10.1061/(asce)gt.1943-5606.0000792.

Mirzababaei, M., Miraftab, M., Mohamed, M. & McMahon, P. (2013[b]). Impact of carpet waste fibre addition on swelling properties of compacted clays. *Geotechnical and Geological Engineering*, 31, No. 1, 173–182, http://dx.doi.org/10.1007/s10706-012-9578-2.

Mirzababaei, M., Mohamed, M., Arulrajah, A., Horpibulsuk, S. & Anggraini, V. (2018[a]). Practical approach to predict the shear strength of fibre–reinforced clay. *Geosynthetics International*, 25, No. 1, 50–66, http://dx.doi.org/10.1680/jgein.17.00033.

Mukherjee, K. & Mishra, A. K. (2017) The impact of scrapped tyre chips on the mechanical properties of liner materials. *Environmental Processes*, 4, No. 1, 219–233, http://dx.doi.org/10.1007/s40710-017-0210-6.

Mukherjee, K. & Mishra, A. K. (2018) Hydraulic and mechanical characteristics of compacted sand–bentonite: Tyre chips mix for its landfill application. *Environment*,

Development and Sustainability, in press, http://dx.doi.org/10.1007/s10668-018-0094-2.

Özkul, Z. H. & Baykal, G. (2006) Shear strength of clay with rubber fiber inclusions. *Geosynthetics International*, 13, No. 5, 173–180, http://dx.doi.org/10.1680/gein.2006.13.5.173.

Özkul, Z. H. & Baykal, G. (2007). Shear behavior of compacted rubber fiber–clay composite in drained and undrained loading. *Journal of Geotechnical and Geoenvironmental Engineering*, 133, No. 7, 767–781, http://dx.doi.org/10.1061/(asce)1090-0241(2007)133:7(767).

Parghi, A. & Alam, M. S. (2016). Physical and mechanical properties of cementitious composites containing recycled glass powder (RGP) and styrene butadiene rubber (SBR). *Construction and Building Materials*, 104, 34–43, http://dx.doi.org/10.1016/j.conbuildmat.2015.12.006.

Perez, J. L., Kwok, C. Y. & Senetakis, K. (2016). Effect of rubber size on the behaviour of sand–rubber mixtures: A numerical investigation. *Computers and Geotechnics*, 80, 199–214, http://dx.doi.org/10.1016/j.compgeo.2016.07.005.

Perez, J. L., Kwok, C. Y. & Senetakis, K. (2017). Investigation of the micromechanics of sand–rubber mixtures at very small strains. *Geosynthetics International*, 24, No. 1, 30–44, http://dx.doi.org/10.1680/jgein.16.00013.

Prakash, K. & Sridharan, A. (2004). Free swell ratio and clay mineralogy of fine–grained soils. *Geotechnical Testing Journal*, 27, No. 2, 220–225, http://dx.doi.org/10.1520/gtj10860.

Prakash, K., Sridharan, A. & Prasanna, H. S. (2009) A note on the determination of plastic limit of fine–grained soils. *Geotechnical Testing Journal*, 32, No. 4, 372–374, http://dx.doi.org/10.1520/gtj101960.

Puppala, A. J., Hoyos, L. R. & Potturi, A. K. (2011). Resilient Moduli Response of Moderately Cement-Treated Reclaimed Asphalt Pavement Aggregates. *Journal of Materials in Civil Engineering*, 23, No. 7, 990–998, http://dx.doi.org/10.1061/(asce)mt.1943-5533.0000268.

Qu, J. & Zhao, D. (2016). Stabilising the cohesive soil with palm fibre sheath strip. *Road Materials and Pavement Design*, 17, No. 1, 87–103, http://dx.doi.org/10.1080/14680629.2015.1064010.

Qu, J., Li, C., Liu, B., Chen, X., Li, M. & Yao, Z. (2013). Effect of random inclusion of wheat straw fibers on shear strength characteristics of Shanghai cohesive soil. *Geotechnical and Geological Engineering*, 31, No. 2, 511–518, http://dx.doi.org/10.1007/s10706-012-9604-4.

Rao, A. S., Phanikumar, B. R. & Sharma, R. S. (2004). Prediction of swelling characteristics of remoulded and compacted expansive soils using free swell index. *Quarterly Journal of Engineering Geology and Hydrogeology*, 37, No. 3, 217–226, http://dx.doi.org/10.1144/1470-9236/03-052.

Sezer, A., İnan, G., Recep Yılmaz, H. & Ramyar, K. (2006). Utilization of a very high lime fly ash for improvement of Izmir clay. *Building and Environment*, 41, No. 2, 150–155, http://dx.doi.org/10.1016/j.buildenv.2004.12.009.

Shalaby, A. & Khan, R. A. (2002). Temperature monitoring and compressibility measurement of a tire shred embankment: Winnipeg, Manitoba, Canada.

Transportation Research Record: Journal of the Transportation Research Board, 1808, 67–75, http://dx.doi.org/10.3141/1808-08.

Signes, C. H., Garzón-Roca, J., Fernández, P. M., Torre, M. E. G. & Franco, R. I. (2016). Swelling potential reduction of Spanish argillaceous marlstone Facies Tap soil through the addition of crumb rubber particles from scrap tyres. *Applied Clay Science*, 132–133, 768–773, http://dx.doi.org/10.1016/j.clay.2016.07.027.

Simon, V., Weigand, B. & Gomaa, H. (2017). Dimensional Analysis for Engineers (1st Ed.). Springer International Publishing AG, Gewerbestrasse, Cham, Switzerland, http://dx.doi.org/10.1007/978-3-319-52028-5. ISBN: 9783319520285.

Soltani, A., Deng, A. & Taheri, A. (2018[a]). Swell–compression characteristics of a fiber–reinforced expansive soil. *Geotextiles and Geomembranes*, 46, No. 2, 183–189, http://dx.doi.org/10.1016/j.geotexmem.2017.11.009.

Soltani, A., Deng, A., Taheri, A. & Mirzababaei, M. (2017[a]). A sulphonated oil for stabilisation of expansive soils. *International Journal of Pavement Engineering*, in press, http://dx.doi.org/10.1080/10298436.2017.1408270.

Soltani, A., Deng, A., Taheri, A. & Mirzababaei, M. (2018[b]). Rubber powder–polymer combined stabilization of South Australian expansive soils. *Geosynthetics International*, 25, No. 3, 304–321, http://doi.org/10.1680/jgein.18.00009.

Soltani, A., Deng, A., Taheri, A. & Sridharan, A. (2018[c]). Swell–shrink–consolidation behavior of rubber–reinforced expansive soils. *Geotechnical Testing Journal*, in press, http://doi.org/10.1520/gtj20170313.

Soltani, A., Deng, A., Taheri, A. & Sridharan, A. (2018[d]) Consistency limits and compaction characteristics of clay soils containing rubber waste. *Proceedings of the Institution of*

Civil Engineers–Geotechnical Engineering, in press, http://dx.doi.org/10.1680/jgeen.18.00042.

Soltani, A., Deng, A., Taheri, A., Sridharan, A. & Estabragh, A. R. (2018[e]). A framework for interpretation of the compressibility behavior of soils. *Geotechnical Testing Journal*, 41, No. 1, 1–16, http://dx.doi.org/10.1520/gtj20170088.

Soltani, A., Taheri, A., Khatibi, M. & Estabragh, A. R. (2017[b]). Swelling potential of a stabilized expansive soil: A comparative experimental study. *Geotechnical and Geological Engineering*, 35, No. 4, 1717–1744, http://dx.doi.org/10.1007/s10706-017-0204-1.

Stark, T. D., Ebeling, R. M. & Vettel, J. J. (1994). Hyperbolic stress–strain parameters for silts. *Journal of Geotechnical Engineering*, 120, No. 2, 420–441, http://dx.doi.org/10.1061/(asce)0733-9410(1994)120:2(420).

Tanchaisawat, T., Voottipruex, P., Bergado, D. T. & Hayashi, S. (2008). Performance of full scale test embankment with reinforced lightweight geomaterials on soft ground. *Lowland Technology International*, 10, No. 1, 84–92.

Tang, C. S., Shi, B. & Zhao, L. Z. (2010). Interfacial shear strength of fiber reinforced soil. *Geotextiles and Geomembranes*, 28, No. 1, 54–62, http://dx.doi.org/10.1016/j.geotexmem.2009.10.001.

Tang, C. S., Shi, B., Gao, W., Chen, F. & Cai, Y. (2007). Strength and mechanical behavior of short polypropylene fiber reinforced and cement stabilized clayey soil. *Geotextiles and Geomembranes*, 25, No. 3, 194–202, http://dx.doi.org/10.1016/j.geotexmem.2006.11.002.

Tatlisoz, N., Benson, C. H. & Edil, T. B. (1997) Effect of fines on mechanical properties of soil–tire chip mixtures. In: *Testing Soil Mixed with Waste or Recycled Materials*

(ASTM STP1275), Wasemiller, M. A. & Hoddinott, K. B., Eds., ASTM International, West Conshohocken, Pennsylvania, USA, http://dx.doi.org/10.1520/stp15645s.

Thomas, B. S., Gupta, R. C. & Panicker, V. J. (2016). Recycling of waste tire rubber as aggregate in concrete: Durability–related performance. *Journal of Cleaner Production*, 112, No. 1, 504–513, http://dx.doi.org/10.1016/j.jclepro.2015.08.046.

Trouzine, H., Bekhiti, M. & Asroun, A. (2012). Effects of scrap tyre rubber fibre on swelling behaviour of two clayey soils in Algeria. *Geosynthetics International*, 19, No. 2, 124–132, http://dx.doi.org/10.1680/gein.2012.19.2.124.

Tsoi, W. Y. & Lee, K. M. (2011). Mechanical properties of cemented scrap rubber tyre chips. *Géotechnique*, 61, No. 2, 133–141, http://dx.doi.org/10.1680/geot.9.p.033.

Tweedie, J. J., Humphrey, D. N. & Sandford, T. C. (1998). Full–scale field trials of tire shreds as lightweight retaining wall backfill under at–rest conditions. *Transportation Research Record: Journal of the Transportation Research Board*, 1619, 64–71, http://dx.doi.org/10.3141/1619-08.

Valdes, J. R. & Evans, T. M. (2008). Sand–rubber mixtures: Experiments and numerical simulations. *Canadian Geotechnical Journal*, 45, No. 4, 588–595, http://dx.doi.org/10.1139/t08-002.

Wang, C., Deng, A. & Taheri, A. (2018) Three–dimensional discrete element modeling of direct shear test for granular rubber–sand. *Computers and Geotechnics*, 97, 204–216, http://dx.doi.org/10.1016/j.compgeo.2018.01.014.

Wang, Y. X., Guo, P. P., Ren, W. X., Yuan, B. X., Yuan, H. P., Zhao, Y. L., Shan, S. B. & Cao, P. (2017). Laboratory investigation on strength characteristics of expansive soil treated with jute fiber reinforcement. *International Journal of Geomechanics*, 17, No.

11, 04017101:1–04017101:12, http://dx.doi.org/10.1061/(asce)gm.1943-5622.0000998.

Williamson, S. & Cortes, D. D. (2014). Dimensional analysis of soil–cement mixture performance. *Géotechnique Letters*, 4, No. 1, 33–38, http://dx.doi.org/10.1680/geolett.13.00082.

Yadav, J. S. & Tiwari, S. K. (2017[a]). The impact of end–of–life tires on the mechanical properties of fine–grained soil: A Review. *Environment, Development and Sustainability*, in press, http://dx.doi.org/10.1007/s10668-017-0054-2.

Yadav, J. S. & Tiwari, S. K. (2017[b]). Effect of waste rubber fibres on the geotechnical properties of clay stabilized with cement. *Applied Clay Science*, 149, 97–110, http://dx.doi.org/10.1016/j.clay.2017.07.037.

Yesilata, B., Isıker, Y. & Turgut, P. (2009). Thermal insulation enhancement in concretes by adding waste PET and rubber pieces. *Construction and Building Materials*, 23, 1878–1882, http://dx.doi.org/10.1016/j.conbuildmat.2008.09.014.

Yoon, S., Prezzi, M., Siddiki, N. Z. & Kim, B. (2006). Construction of a test embankment using a sand–tire shred mixture as fill material. *Waste Management*, 26, No. 9, 1033–1044, http://dx.doi.org/10.1016/j.wasman.2005.10.009.

Youwai, S. & Bergado, D. T. (2004). Numerical analysis of reinforced wall using rubber tire chips–sand mixtures as backfill material. *Computers and Geotechnics*, 31, No. 2, 103–114, http://dx.doi.org/10.1016/j.compgeo.2004.01.008.

Zhang, T., Cai, G. & Duan, W. (2017). Strength and microstructure characteristics of the recycled rubber tire–sand mixtures as lightweight backfill. *Environmental Science and Pollution Research*, in press, http://dx.doi.org/10.1007/s11356-017-0742-3.

Zhao, Y., Gao, Y., Zhang, Y. & Wang, Y. (2016). Effect of fines on the mechanical properties of composite soil stabilizer–stabilized gravel soil. *Construction and Building Materials*, 126, 701–710, http://dx.doi.org/10.1016/j.conbuildmat.2016.09.082.

Zornberg, J. G., Cabral, A. R. & Viratjandr, C. (2004). Behaviour of tire shred–sand mixtures. *Canadian Geotechnical Journal*, 41, No. 2, 227–241, http://dx.doi.org/10.1139/t03-086.

Table captions

Table 1. Physical and mechanical properties of the soil.
Table 2. Basic index properties of the prepared samples.

Table 3. Shear strength parameters at peak condition for the tested samples.

Table 4. Summary of the regression analysis outputs with respect to the proposed dimensional model M_1 (Equation 14) for both rubber types.

Table 5. Summary of the regression analysis outputs with respect to the proposed dimensional model M_2 (Equation 17) for both rubber types.

Table 6. Summary of the regression analysis outputs with respect to the proposed dimensional model M_3 (Equation 20) for both rubber types.

Accepted manuscript doi:
10.1680/jgein.18.00045

Table 1. Physical and mechanical properties of the soil.

Properties	Value/Description	Standard designation
Specific gravity, G_s	2.73	ASTM D854 (2014)
Grain–size distribution		
Clay (< 2 μm) (%)	52.80	ASTM D422 (2007)
Silt (2–75 μm) (%)	46.16	
Fine sand (0.075–0.425 mm) (%)	1.04	
Medium sand (0.425–2 mm) (%)	0	
Coarse sand (2–4.75 mm) (%)	0	
Consistency limits		
Liquid limit, w_L (%)	59.60	AS 1289.3.9.1 (2015)[a]
Plastic limit, w_P (%)	27.28	AS 1289.3.2.1 (2009)[b]
Plasticity index, I_P (=w_L–w_P) (%)	32.32	AS 1289.3.3.1 (2009)
Linear shrinkage, w_S (%)	8.19	AS 1289.3.4.1 (2008)
Classifications		
USCS classification	CH	ASTM D2487 (2011)
Free swell ratio, FSR[c]	2.91	Prakash and Sridharan (2004)
Expansive potential	High	
Compaction characteristics		
Optimum water content, w_{opt} (%)	26.00	ASTM D698 (2012)
Maximum dry unit weight, γ_{dmax} (kN/m^3)	15.07	

Notes:
[a]Cone penetration method; [b]Rolling thread method; and [c]Ratio of equilibrium sediment volume of 10 g oven–dried soil passing sieve 425 μm in distilled water to that of kerosene.

Table 2. Basic index properties of the prepared samples.

Rubber	R_c (%)[a]	w_L (%)	w_P (%)	I_P (%)	w_{opt} (%)[b]	γ_{dmax} (kN/m^3)[b]
—	0	59.60	27.28	32.32	26.00	15.07
Rubber C	5	57.03	27.02	30.01	24.77	14.63
	10	55.04	25.54	29.50	23.87	14.35
	20	51.51	23.46	28.05	21.85	13.87
	30	49.58	22.70	26.88	20.07	13.52
Rubber B	5	56.88	26.61	30.27	24.47	14.61
	10	55.62	24.77	30.85	23.46	14.37
	20	52.44	23.27	29.17	21.15	13.86
	30	51.21	22.15	29.06	19.94	13.52

Notes:
[a]R_c=W_r/W_s×100 (W_r=weight of rubber particles; and W_s=weight of soil solids); and [b]Initial placement condition for direct shear tests.

Accepted manuscript doi:
10.1680/jgein.18.00045

Table 3. Shear strength parameters at peak condition for the tested samples.

Rubber	R_c **(%)**	c_p **(kPa)**	φ_p **(°)**
—	0	58.35	9.64
Rubber C	5	59.03	10.63
	10	62.25	13.28
	20	75.89	15.72
	30	98.47	16.56
Rubber B	5	61.86	10.97
	10	71.26	13.33
	20	76.06	14.55
	30	86.19	15.30

Table 4. Summary of the regression analysis outputs with respect to the proposed dimensional model M_1 (Equation 14) for both rubber types.

Rubber	**Variable**	β_o	β_1	R^2	**RMSE (kPa)**	**MAPE (%)**
Rubber C	τ_p (Pa)	–0.099	0.127	0.975	8.59	5.43
	τ_{cr} (Pa)	–0.017	0.080	0.985	4.99	3.75
Rubber B	τ_p (Pa)	–0.063	0.230	0.946	11.29	6.21
	τ_{cr} (Pa)	–0.055	0.183	0.979	7.05	5.21

Table 5. Summary of the regression analysis outputs with respect to the proposed dimensional model M_2 (Equation 17) for both rubber types.

Rubber	**Variable**	β_o	β_1	R^2	**RMSE (kPa)**	**MAPE (%)**
Rubber C	τ_p (Pa)	0.759	–1.17	0.978	7.68	4.78
	τ_{cr} (Pa)	0.526	–1.04	0.987	4.88	3.52
Rubber B	τ_p (Pa)	1.489	–1.10	0.946	10.79	6.53
	τ_{cr} (Pa)	1.176	–1.11	0.976	7.49	5.65

Table 6. Summary of the regression analysis outputs with respect to the proposed dimensional model M_3 (Equation 20) for both rubber types.

Rubber	**Variable**	β_o	β_1	β_2	R^2	**RMSE (kPa)**	**MAPE (%)**
Rubber C	τ_p (Pa)	–0.90	–1.10	–1.25	0.988	6.56	4.06
	τ_{cr} (Pa)	–1.13	–0.51	–1.00	0.988	4.16	3.37
Rubber B	τ_p (Pa)	–0.64	–1.68	–1.23	0.979	7.02	4.36
	τ_{cr} (Pa)	–1.33	–1.08	–1.04	0.984	5.92	4.10

Accepted manuscript doi:
10.1680/jgein.18.00045

Figure captions

Figure 1. Gradation curves for the used materials.

Figure 2. Tire rubbers at different magnification ratios: (a) Rubber C (no magnification); (b) Rubber C (50x magnification); (c) Rubber C (200x magnification); (d) Rubber B (no magnification); (e) Rubber B (50x magnification); and (f) Rubber B (200x magnification).

Figure 3. Typical shear stress–horizontal displacement curves at σ_n=200 kPa: (a) Rubber C; and (b) Rubber B.

Figure 4. Variations of shear strength against normal stress for the tested samples: (a) Peak shear strength τ_p; and (b) Critical shear strength τ_{cr}.

Figure 5. Variations of the dependent Pi term π_o (Equation 2) against the first dimensionless shear number η_1 (Equation 13) at both peak and critical state conditions: (a) Rubber C; and (b) Rubber B.

Figure 6. Predicted (by Model M_1 or Equation 14) versus actual data, along with the corresponding 95% prediction bands, for various soil–rubber composites: (a) Peak shear strength τ_p; and (b) Critical shear strength τ_{cr}.

Figure 7. Variations of the dependent Pi term π_o (Equation 2) against the second dimensionless shear number η_2 (Equation 16) at both peak and critical state conditions: (a) Rubber C; and (b) Rubber B.

Figure 8. Predicted (by Model M_2 or Equation 17) versus actual data, along with the corresponding 95% prediction bands, for various soil–rubber composites: (a) Peak shear strength τ_p; and (b) Critical shear strength τ_{cr}.

Figure 9. Variations of both predicted (by Model M_3 or Equation 20) and actual τ_p and τ_{cr} data against normal stress: (a) Rubber C; and (b) Rubber B.

Figure 10. Predicted (by Model M_3 or Equation 20) versus actual data, along with the corresponding 95% prediction bands, for various soil–rubber composites: (a) Peak shear strength τ_p; and (b) Critical shear strength τ_{cr}.

Figure 11. Variations of both predicted (by Equation 22) and actual shear stress data against normal stress at various horizontal displacements.

Figure 12. Typical experimental shear stress–horizontal displacement curves along with their respective simulations by means of the proposed dimensional model given in Equation 22.

Accepted manuscript doi:
10.1680/jgein.18.00045

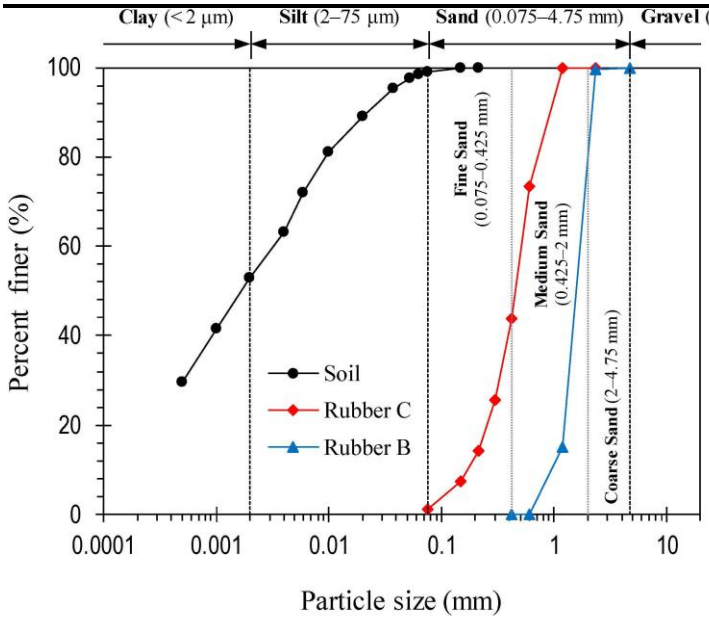

Variable	Rubber C
d_{10} (mm)	0.182
d_{30} (mm)	0.334
d_{50} (mm)	0.478
d_{60} (mm)	0.513
C_c	1.20
C_u	2.81
Variable	**Rubber B**
d_{10} (mm)	1.077
d_{30} (mm)	1.370
d_{50} (mm)	1.582
d_{60} (mm)	1.682
C_c	1.04
C_u	1.56

Figure 1

Accepted manuscript doi:
10.1680/jgein.18.00045

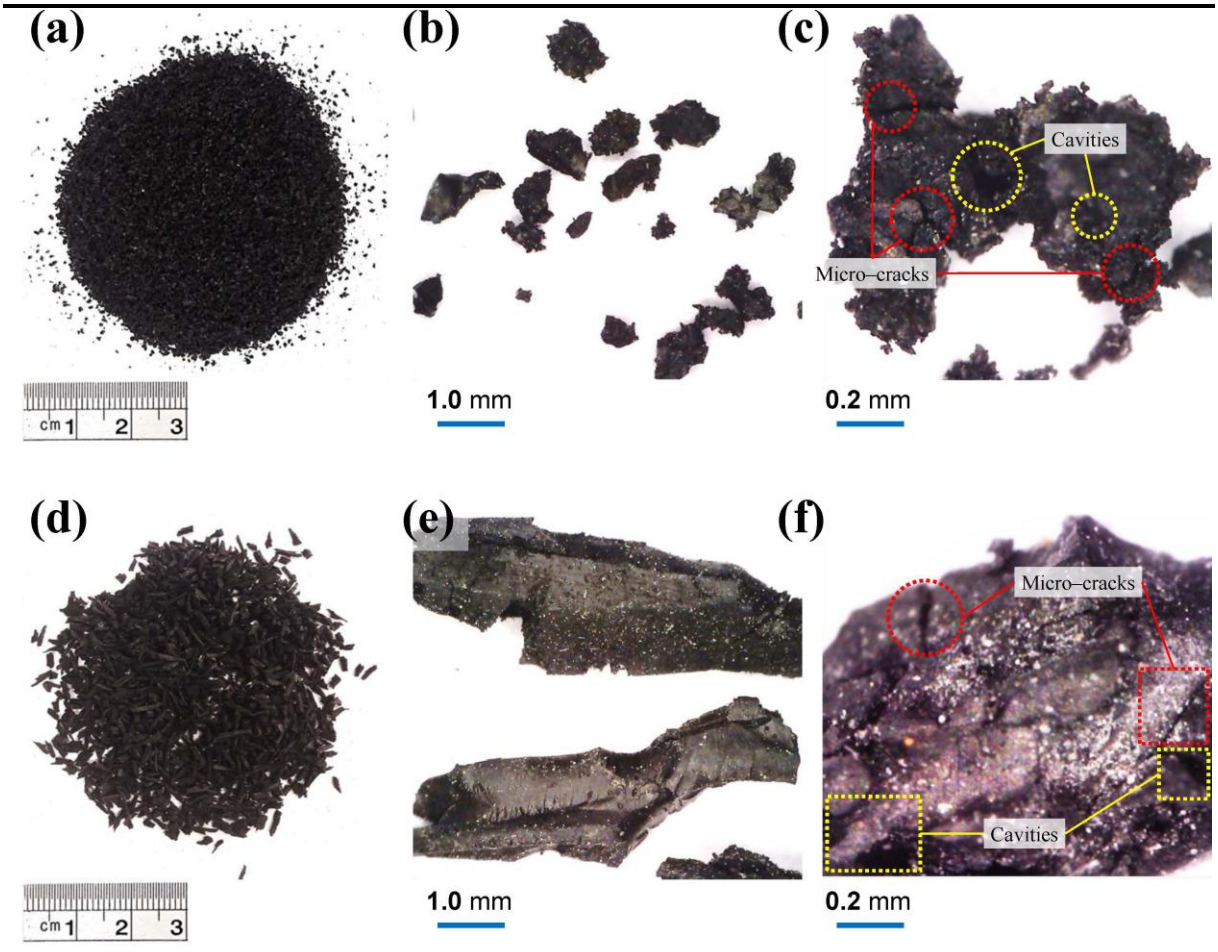

Figure 2.

Accepted manuscript doi:
10.1680/jgein.18.00045

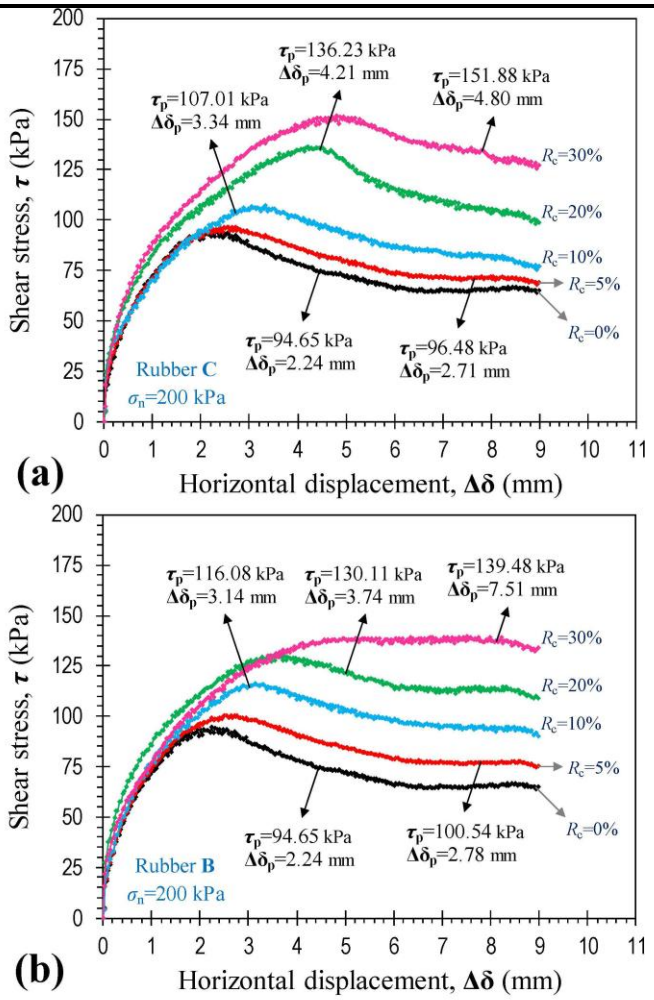

Figure 3

Accepted manuscript doi:
10.1680/jgein.18.00045

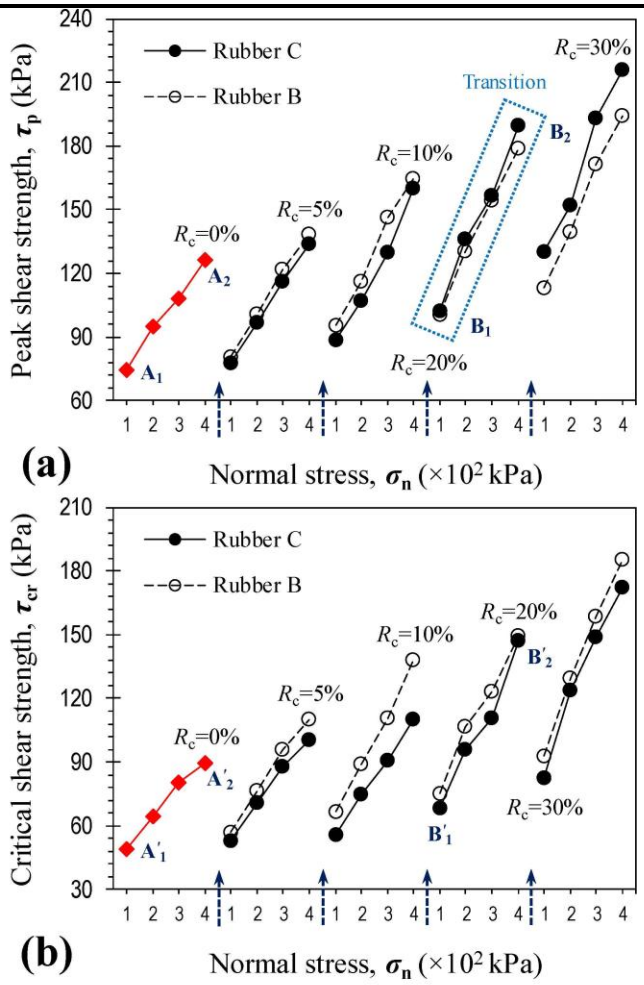

Figure 4.

Accepted manuscript doi:
10.1680/jgein.18.00045

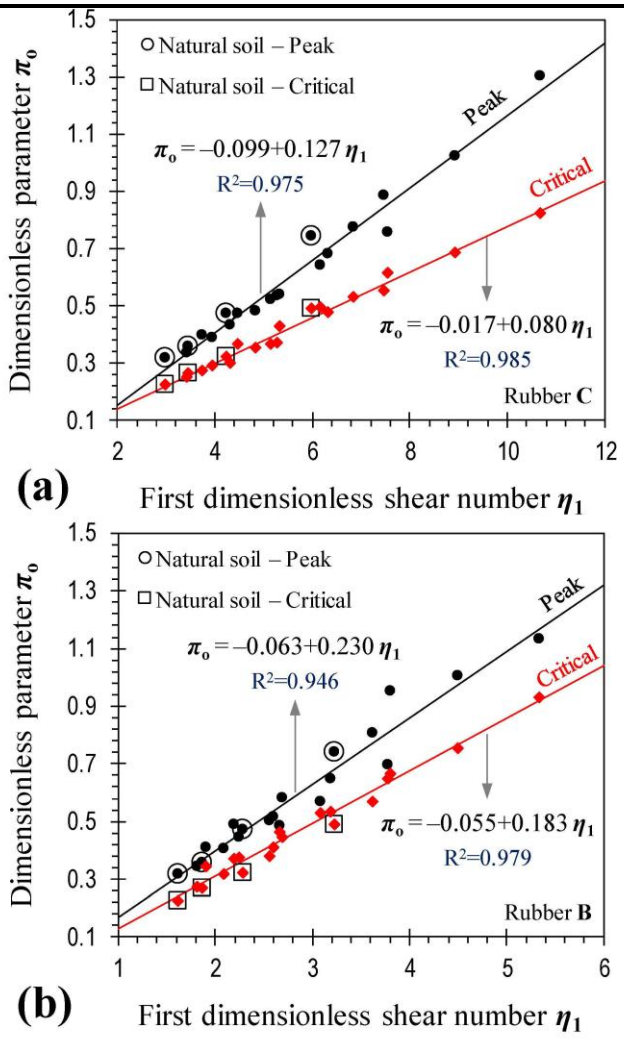

Figure 5

Accepted manuscript doi:
10.1680/jgein.18.00045

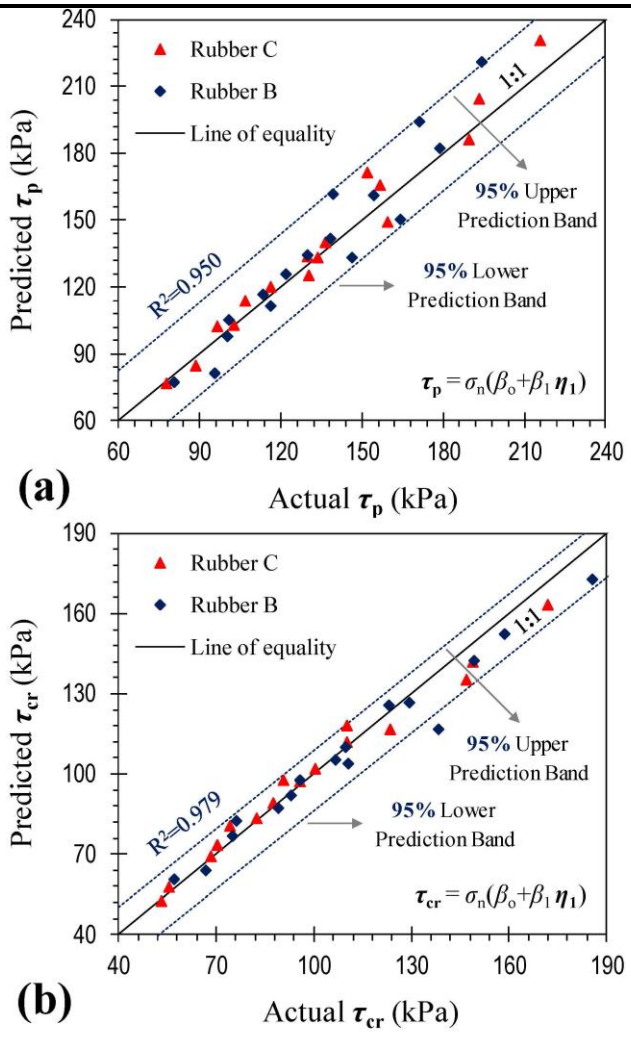

Figure 6.

Accepted manuscript doi:
10.1680/jgein.18.00045

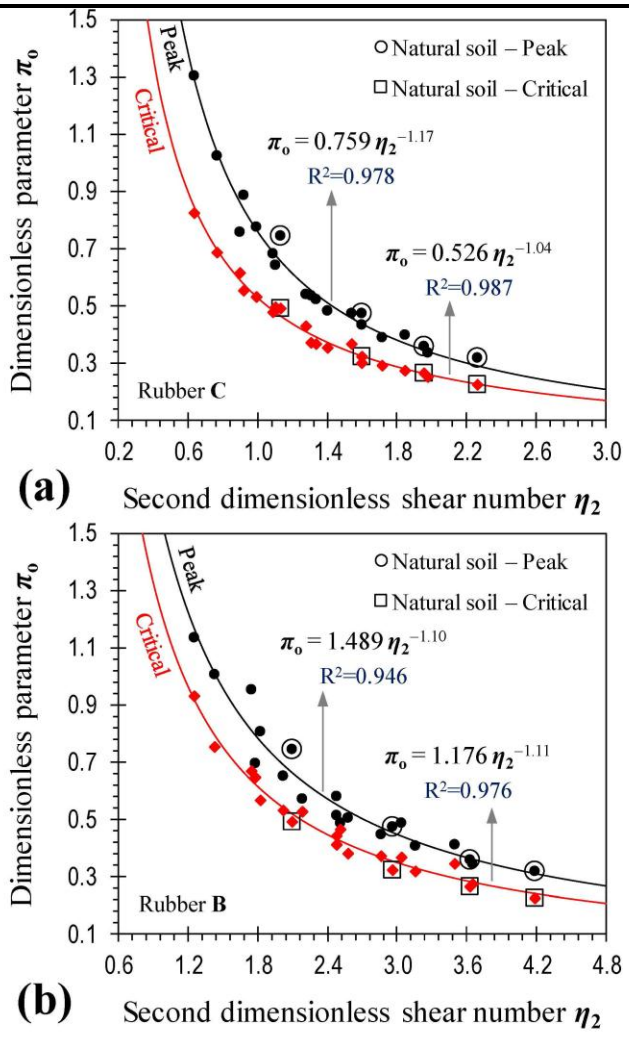

Figure 7.

Accepted manuscript doi:
10.1680/jgein.18.00045

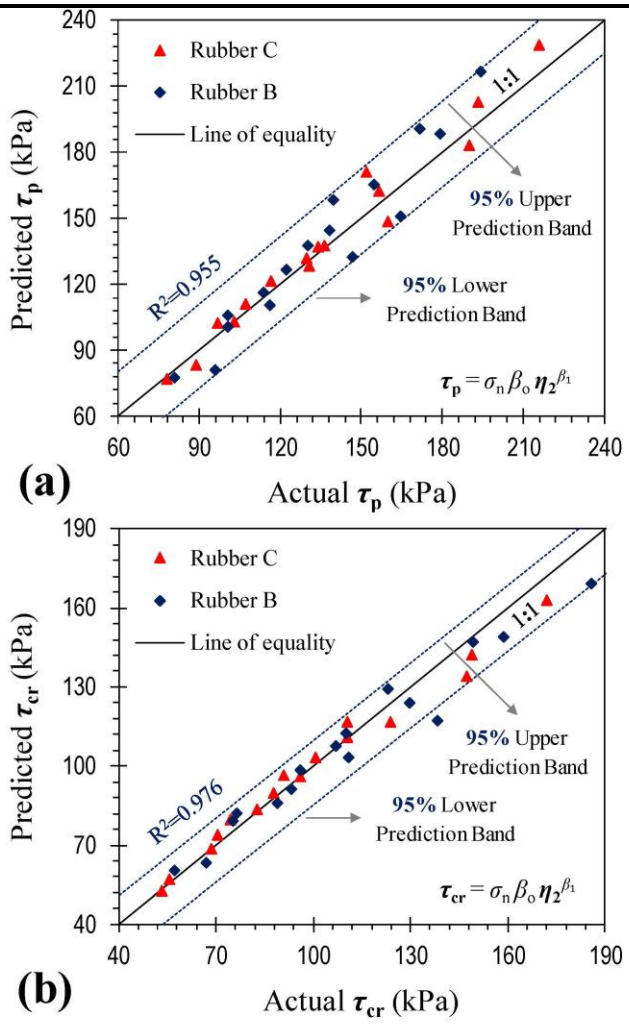

Figure 8

Accepted manuscript doi:
10.1680/jgein.18.00045

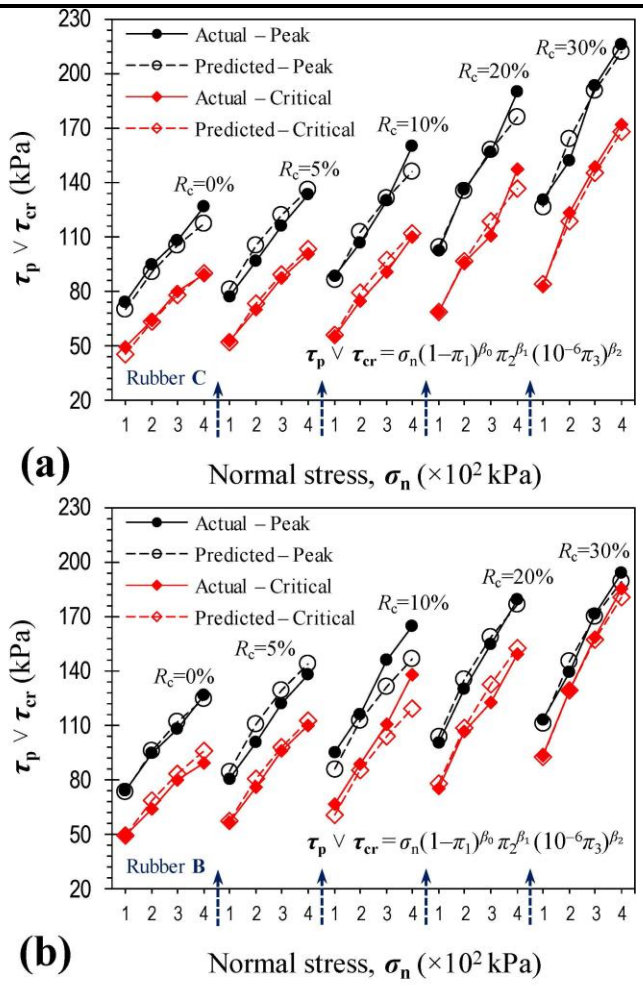

Figure 9

Accepted manuscript doi:
10.1680/jgein.18.00045

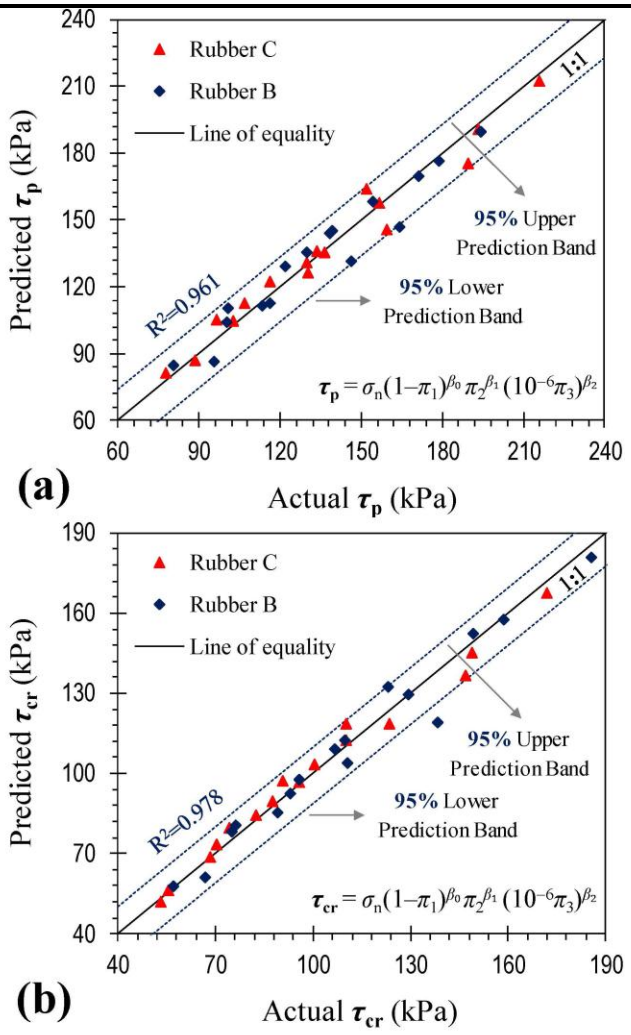

Figure 10.

Accepted manuscript doi:
10.1680/jgein.18.00045

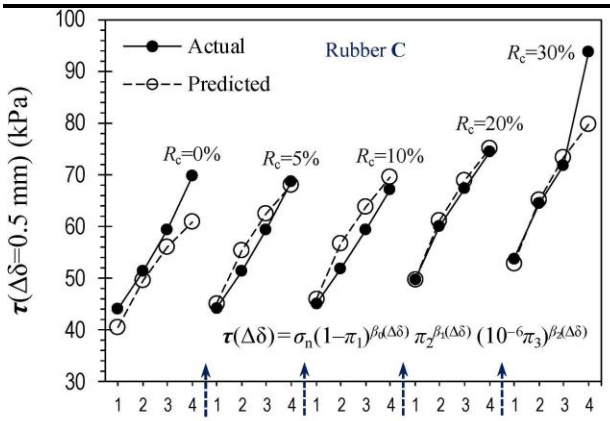

Rubber C: Δδ=0.5 mm

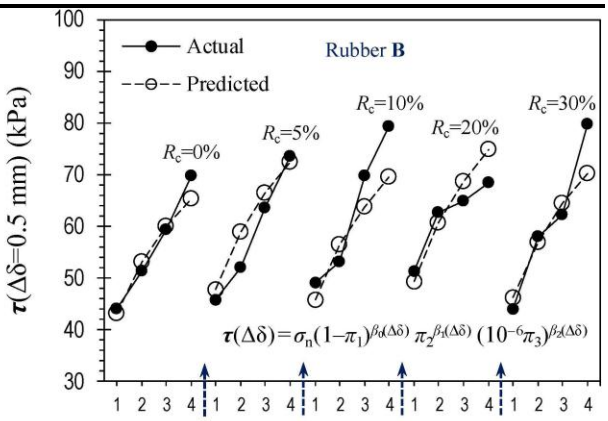

Rubber B: Δδ=0.5 mm

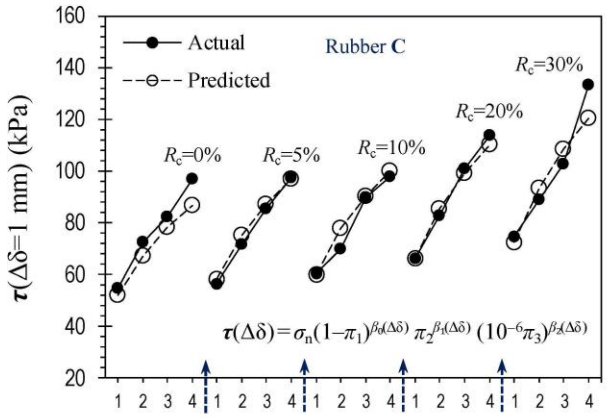

Rubber C: Δδ=1 mm

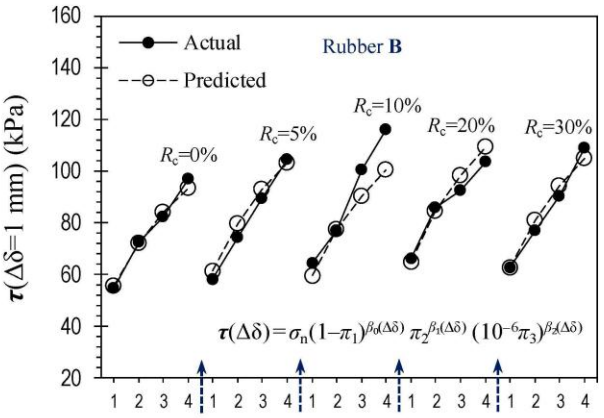

Rubber B: Δδ=1 mm

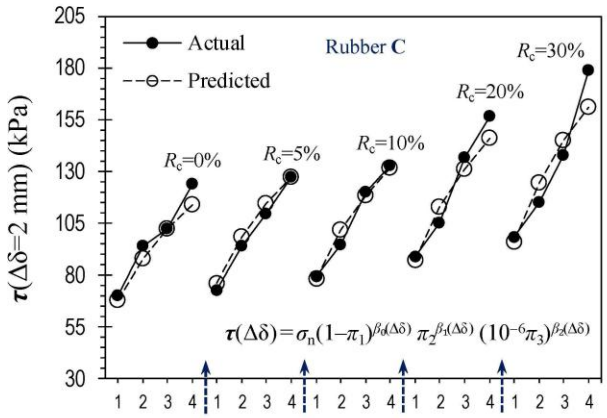

Rubber C: Δδ=2 mm

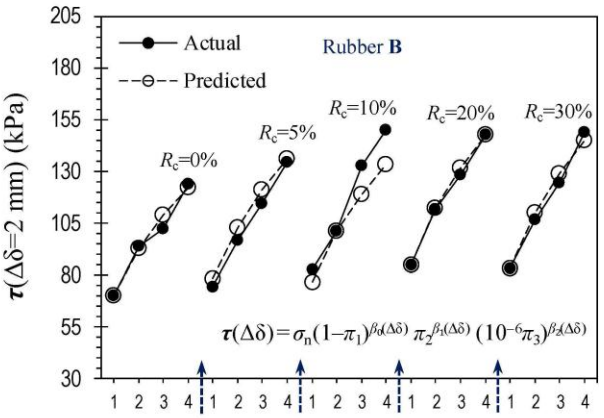

Rubber B: Δδ=2 mm

Accepted manuscript doi:
10.1680/jgein.18.00045

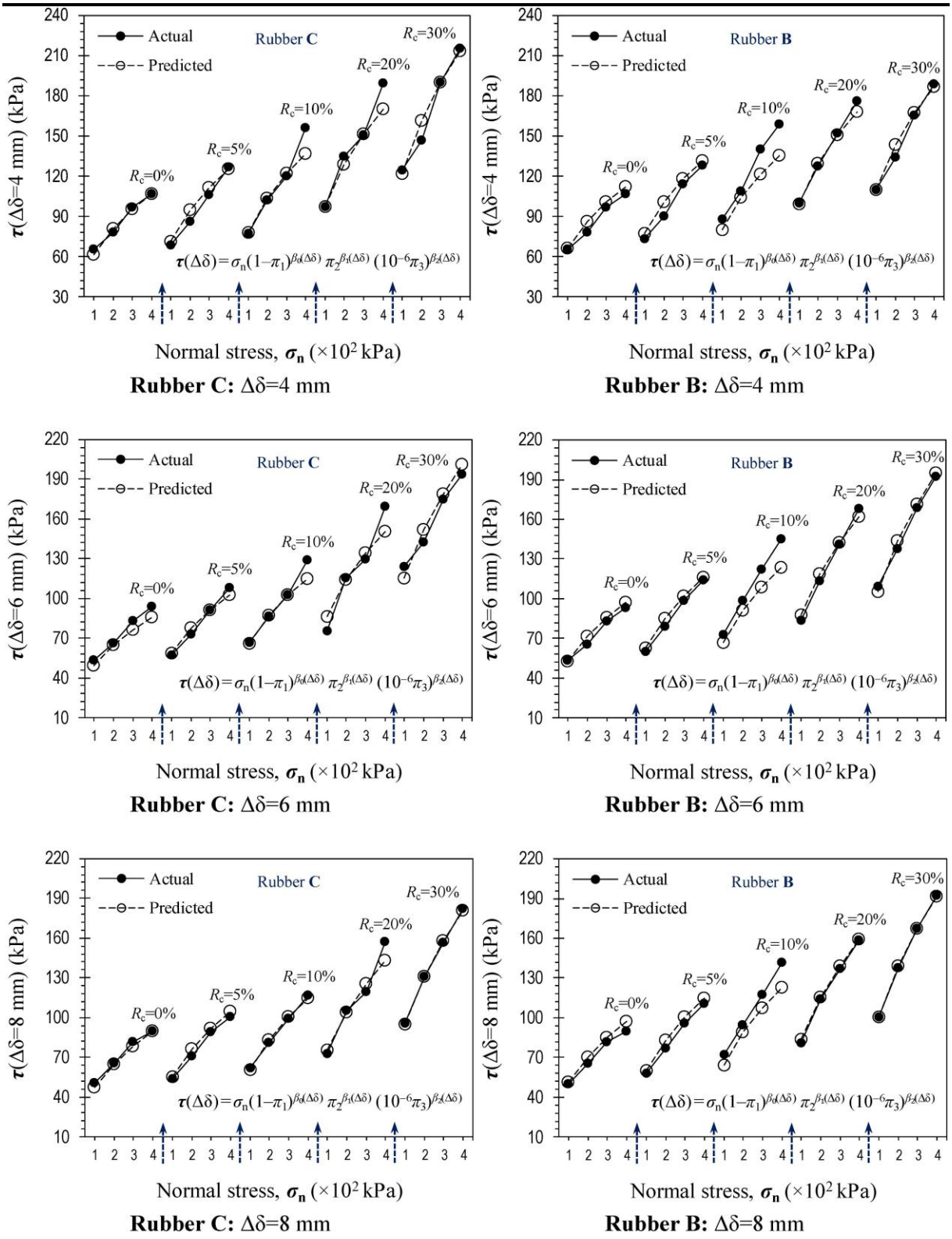

Rubber C: Δδ=4 mm **Rubber B:** Δδ=4 mm

Rubber C: Δδ=6 mm **Rubber B:** Δδ=6 mm

Rubber C: Δδ=8 mm **Rubber B:** Δδ=8 mm

Figure 11

Accepted manuscript doi:
10.1680/jgein.18.00045

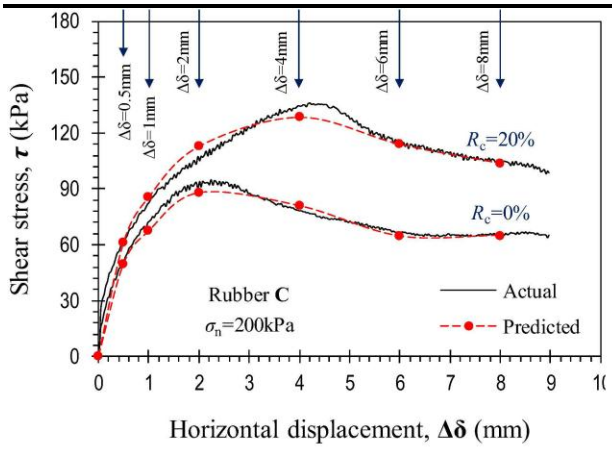

Rubber C: R_c=0% and 20%; and σ_n=200 kPa

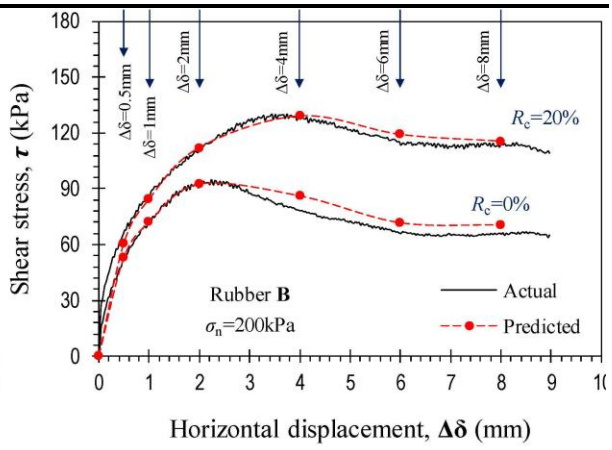

Rubber B: R_c=0% and 20%; and σ_n=200 kPa

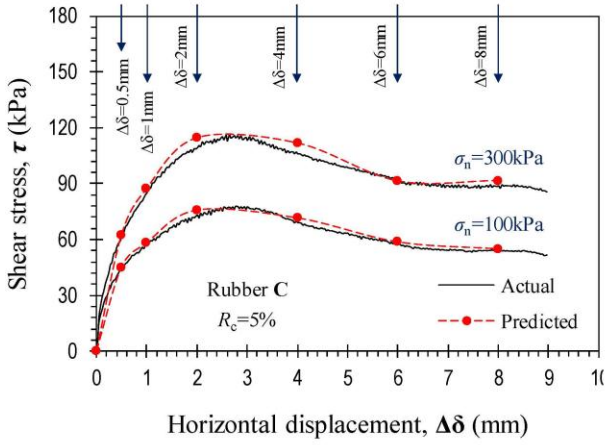

Rubber C: R_c=5%; and σ_n=100 kPa and 300 kPa

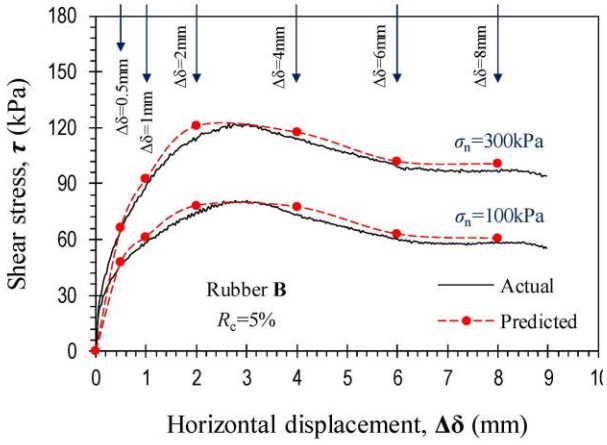

Rubber B: R_c=5%; and σ_n=100 kPa and 300 kPa

Figure 12